

Fulfillment of sum rules and Ward identities in the multiloop functional renormalization group solution of the Anderson impurity model

Patrick Chalupa-Gantner ¹, Fabian B. Kugler ², Cornelia Hille ³, Jan von Delft ⁴,
Sabine Andergassen ³ and Alessandro Toschi ¹

¹*Institute of Solid State Physics, TU Wien, 1040 Vienna, Austria*

²*Department of Physics and Astronomy, Rutgers University, Piscataway, New Jersey 08854, USA*

³*Institut für Theoretische Physik and Center for Quantum Science, Universität Tübingen, Auf der Morgenstelle 14, 72076 Tübingen, Germany*

⁴*Arnold Sommerfeld Center for Theoretical Physics, Center for NanoScience, and Munich Center for Quantum Science and Technology, Ludwig-Maximilians-Universität München, 80333 Munich, Germany*



(Received 15 October 2021; revised 22 March 2022; accepted 23 March 2022; published 20 April 2022)

We investigate several fundamental characteristics of the multiloop functional renormalization group (mfRG) flow by means of its application to a prototypical many-electron system: the Anderson impurity model (AIM). We first analyze the convergence of the algorithm in the different parameter regions of the AIM. As no additional approximation is made, the multiloop series for the local self-energy and response functions converge perfectly to the corresponding results of the parquet approximation (PA) in the weak- to intermediate-coupling regime. Small oscillations of the mfRG solution as a function of the loop order gradually increase with the interaction, hindering a full convergence to the PA in the strong-coupling regime, where perturbative resummation schemes are no longer reliable. By exploiting the converged results, we inspect the fulfillment of (i) sum rules associated to the Pauli principle and (ii) Ward identities related to conservation laws. For the Pauli principle, we observe a systematic improvement by increasing the loop order and including the multiloop corrections to the self-energy. This is consistent with the preservation of crossing symmetries and two-particle self-consistency in the PA. For the Ward identities, we numerically confirm a visible improvement by means of the Katanin substitution. At weak coupling, violations of the Ward identity are further reduced by increasing the loop order in mfRG. In this regime, we also determine the precise scaling of the deviations of the Ward identity as a function of the electronic interaction. For larger interaction values, the overall behavior becomes more complex, and the benefits of the higher-loop terms are mostly present in the contributions at large frequencies.

DOI: [10.1103/PhysRevResearch.4.023050](https://doi.org/10.1103/PhysRevResearch.4.023050)

I. INTRODUCTION

The many-electron problem poses a formidable challenge to modern solid-state physics, involving a large number of degrees of freedom at different energy scales. In general, although the exact solution cannot be computed, some of its fundamental properties are known *a priori*. Specifically, the exact solution is guaranteed to obey the Pauli principle, which manifests itself in sum rules and the crossing symmetry of four-point correlators. At the same time, it also fulfills Ward identities (WIs) related to thermodynamic and quantum-mechanical principles. This knowledge usually provides an important “compass” for constructing suitable approximation schemes. For a given approximation, however, the preservation of *all* fundamental features of the exact solution cannot be guaranteed [1]. For instance, approximate schemes constructed from the Luttinger-Ward functional, so-called

conserving approximations, maintain WIs—an important aspect when comparing with spectroscopic experiments—but violate the crossing symmetries. On the other hand, it is known that approximate approaches specifically designed to guarantee the crossing symmetries, such as the parquet approximation (PA) [1–6], violate the WIs to a certain degree [7–9]. Hence, investigating how this trade-off actually manifests itself in advanced quantum many-body methods will provide significant theoretical insight.

In this paper, we analyze these issues within the functional renormalization group (fRG) for interacting Fermi systems [10–14], which can be used as a framework for introducing powerful new approximation schemes. Specifically, we consider the recent multiloop extension (mfRG) of fermionic fRG in the vertex expansion [9,15,16] and apply it to the Anderson impurity model (AIM), a paradigmatic model of many-body physics. Reasons for focusing on this particular model are given below.

Computation schemes based on the fermionic fRG can be designed to treat the characteristic scale-dependent behavior of correlated electrons in a flexible and unbiased way. The most commonly used implementations employ the one-loop (1ℓ) truncation of the exact hierarchy of flow equations. There, one neglects three-particle and higher vertices, which can be

Published by the American Physical Society under the terms of the [Creative Commons Attribution 4.0 International](https://creativecommons.org/licenses/by/4.0/) license. Further distribution of this work must maintain attribution to the author(s) and the published article's title, journal citation, and DOI.

justified, e.g., from a perturbative perspective. Several studies have discussed the nonconserving nature of 1ℓ fRG-based schemes, and possible routes for mitigating the violation of the associated WIs have been proposed [10,17–20]. An important example is the widely used Katanin substitution [17]. In its most common form, it incorporates some contributions from the three-particle vertex as two-loop contributions to the flow of the two-particle vertex via (one-particle) self-energy corrections. The Katanin substitution was designed to better fulfill WIs—we here present first numerical results to quantitatively assess this aspect. Conversely, WIs have also been used to propose new truncation schemes [21–23].

The multiloop extension of the fRG approach, mfRG, includes all contributions of the three-particle vertex to the flow of the two-particle vertex and self-energy that can be computed with numerical costs proportional to the 1ℓ flow. In doing so, it sums up all parquet diagrams, formally reconstructing the PA if loop convergence is achieved [9,15,16]. This ensures self-consistency at the one- and two-particle level, in that the PA is a solution of the self-consistent parquet equations [1]. It also ensures the validity of one-particle conservation laws, but not of two-particle ones [9].

Whether or not mfRG yields quantitative improvements over the 1ℓ truncation depends on the context. For a zero-dimensional model with a logarithmically divergent perturbation theory, it was recently shown [24] that the leading logarithms can be obtained in the 1ℓ truncation, in which case the higher-loop contributions incorporated via mfRG thus are subleading. Similarly, 1ℓ fRG treatments of the interacting resonant level model [25–28] as well as inhomogeneous Tomonaga-Luttinger liquids [29–35] should yield a proper summation of the leading logs governing the infrared behavior of these systems. By contrast, a quantitatively precise description of the weakly interacting two-dimensional Hubbard model could only be achieved with a full multiloop computation [36–38]. It is thus of interest to analyze the multiloop series for a model whose perturbation series lacks a leading-log classification, but which is less complex than the Hubbard model.

This criterion is satisfied by the AIM. We study it here at finite temperature in the imaginary-frequency Matsubara formalism. A Matsubara treatment of the AIM suits our purpose for two further reasons. First, a numerically exact solution is available as a benchmark via quantum Monte Carlo (QMC) methods [39]. Second, recent algorithmic and methodological advances [5,6] make it possible to track the full frequency dependence of the two-particle vertex functions of the AIM [40–42], including their nontrivial asymptotic structure [6]. The numerical (m)fRG equations can be then solved to great accuracy and without any further approximations. This sets our study apart from recent mfRG applications [36,37] to more complex systems (where additional approximations for the momentum dependence [43,44] of the problem were necessary) and builds upon previous frequency-dependent fRG studies of the AIM [45–50], paving the way for a systematic inspection of sum rules and WIs in mfRG and parquet approaches.

From a more general perspective, we note that flows of the truncated fermionic fRG or mfRG can *a priori* be expected to be reliable for weak to intermediate interaction strengths

only. However, nonperturbative [51] parameter regimes of, e.g., the Hubbard model can be accessed [52,53] via fRG by proceeding as follows: First evoke dynamical mean-field theory (DMFT) [54] to solve a self-consistent AIM (by non-fRG means, e.g., QMC or the numerical renormalization group [55]); then use fRG to systematically include nonlocal correlations missed by DMFT [42]. This procedure defines the so-called DMF²RG scheme [56,57]. So far, it has been implemented in the 1ℓ truncation, but multiloop extensions are conceivable, too. Our careful investigation of the mfRG solution of the AIM may also provide valuable methodological information for future multiloop DMF²RG developments. For example, analogous vertex frequency parametrizations are needed for a mfRG treatment of the AIM and for the mfRG part of DMF²RG computations. Furthermore, the study of the mfRG convergence properties as well as of crossing symmetries and WIs for different coupling strengths will represent an important guidance for DMF²RG calculations relying on multiloop resummations.

The structure of our paper reflects the main scientific questions raised above. After introducing the required formalism in Sec. II, we present a detailed analysis of the mfRG solution of the AIM in Sec. III. We illustrate how the convergence to the corresponding results of the PA is perfectly achieved in the weak- to intermediate-coupling regime and also discuss the appearance of increasing multiloop oscillations in the strong-coupling regime. Having defined the parameter region of convergence for mfRG applied to the AIM, we analyze in Sec. IV the fulfillment of the sum rules associated to the Pauli principle as well as of the WIs related to conservation laws. We discuss the systematic effects observed as a function of loop order, and separately consider the low- and high-frequency parts of the WIs. Throughout, we also include results obtained via the Katanin substitution, allowing its merits to be compared to those of 1ℓ or higher-loop schemes. We summarize our conclusions and perspectives for future developments in Sec. V, and discuss additional technical aspects relevant to a more specialized readership in the Appendices.

II. FORMALISM

In this section, we concisely introduce the methods and concepts underlying the calculations presented in the following sections. For brevity, we reduce the formal derivations to a minimum, referring to prior works for more explicit discussions. In Sec. IV, we extend the formalism where needed for the analysis of the Pauli principle and WIs.

A. Anderson impurity model

Throughout this paper, we consider the AIM [58] close to the wide-band limit [59]. The Hamiltonian is given by

$$\hat{\mathcal{H}} = \sum_{\sigma} \epsilon_d \hat{d}_{\sigma}^{\dagger} \hat{d}_{\sigma} + \sum_{\mathbf{k}, \sigma} \epsilon_{\mathbf{k}} \hat{c}_{\mathbf{k}, \sigma}^{\dagger} \hat{c}_{\mathbf{k}, \sigma} + U \hat{n}_{\uparrow} \hat{n}_{\downarrow} + \sum_{\mathbf{k}, \sigma} (V_{\mathbf{k}} \hat{d}_{\sigma}^{\dagger} \hat{c}_{\mathbf{k}, \sigma} + \text{H.c.}), \quad (1)$$

where \hat{d}_σ^\dagger (\hat{d}_σ) is the creation (annihilation) operator of electrons localized on the impurity site, and $\hat{c}_{\mathbf{k},\sigma}^\dagger$, $\hat{c}_{\mathbf{k},\sigma}$ are the corresponding operators for the bath electrons. The energy on the impurity site is denoted by ϵ_d and the dispersion relation in the bath by $\epsilon_{\mathbf{k}}$. The first term in the second line represents the local interaction, where U is the interaction strength and $\hat{n}_\sigma = \hat{d}_\sigma^\dagger \hat{d}_\sigma$ with $\sigma \in \{\uparrow, \downarrow\}$. The second term accounts for the hopping onto/off the impurity site, where we consider a \mathbf{k} -independent hybridization strength $V_{\mathbf{k}} = V$. We set $V = 2$, thereby measuring energy in units of $V/2$. We use a box-shaped DOS for the bath electrons, $\rho(\epsilon) = 1/(2D)\Theta(D - |\epsilon|)$, with half-bandwidth $D = 10$. Further, we consider half filling, where $\epsilon_d = -U/2$ is exactly canceled by the Hartree self-energy. Thus, the (bare) propagator is purely imaginary:

$$G_{0,v} = \frac{1}{iv - \Delta_v}, \quad \Delta_v = -i \frac{V^2}{D} \arctan \frac{D}{v}. \quad (2)$$

For $|v| \ll D$, we find $\Delta_v \approx -i \text{sgn}(v) \Delta_0$ with the characteristic hybridization strength $\Delta_0 = \pi V^2 / (2D) = \pi/5 \simeq 0.63$. For prior studies using this specific AIM, see Ref. [60] and especially Ref. [51], where the physical regimes relevant for this paper are also discussed. For a more general introduction of the physics of the AIM, we refer to Refs. [59,61]. The values $U = 1, 1.5, 2, 3$, and 4 studied below correspond to $U/\Delta_0 \simeq 1.59, 2.39, 3.18, 4.77$, and 6.37 , respectively. Throughout we fix the inverse temperature to $\beta = 10$.

B. Numerical approaches

fRG flows and PA—We briefly discuss here the structure of the flow equations, both on the one- and multiloop level, as well as the PA, for the one-particle self-energy Σ , the two-particle vertex F , and the susceptibilities χ of the AIM.

The fRG flow describes the evolution of Σ , F , χ upon tuning the scale or flow parameter Λ from an initial value Λ_i to a final value Λ_f . The flow parameter Λ is introduced in the quadratic part of the action, i.e., the bare (one-particle) propagator [Eq. (2)]. We consider two cutoff functions: the frequency flow (or Ω flow for short),

$$G_{0,v}^\Lambda = \frac{v^2}{v^2 + \Lambda^2} G_{0,v} \quad \text{with } \Lambda_i = \infty, \Lambda_f = 0, \quad (3)$$

and the interaction flow (or U flow) [62],

$$G_{0,v}^\Lambda = \Lambda G_{0,v} \quad \text{with } \Lambda_i = 0, \Lambda_f = 1. \quad (4)$$

With $G_0^{\Lambda_i} = 0$, the initial values of Σ and F are $\Sigma^{\Lambda_i} = 0$, where the Hartree term is absorbed in G_0 , and $F^{\Lambda_i} = F_0$, the bare vertex of magnitude U (in our convention $F_0^{\sigma\sigma'} = -U\delta_{\sigma\sigma'}$, where $\uparrow = \downarrow$ and vice versa). The fRG flow of Σ is determined by the two-particle vertex F contracted with the single-scale propagator $S = -G(\partial_\Lambda G_0^{-1})G$, which is related to the differentiated propagator $\hat{G} \equiv \partial_\Lambda G$ by $\hat{G} = S + G\Sigma G$. For simplicity, we omit the superscript Λ here and henceforth. The flow equation for F further involves the three-particle vertex $\Gamma^{(6)}$. If $\Gamma^{(6)}$ was known at all scales, the flow of Σ and F would be exact. This would imply, in particular, that every specific Λ dependence or cutoff choice, as in Eqs. (3) or (4), yields the same result at the end of the flow. In practice, however, $\Gamma^{(6)}$ can hardly be treated numerically and its effect on the

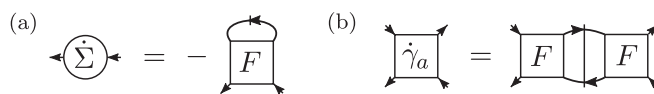


FIG. 1. Diagrammatic representation of the one-loop flow of (a) the self-energy and (b) the vertex in the a channel. The slashed line denotes S , the slashed pair of lines $\hat{\Gamma}_{a,S}$.

flow of Σ and F can only be accounted for approximately. As a consequence, the results of such truncated fRG flows will generically depend on the choice of the cutoff.

The most widely used fRG implementations neglect $\Gamma^{(6)}$, yielding approximate 1ℓ flow equations for Σ and F . The contributions of $\Gamma^{(6)}$ that amount to self-energy derivatives can be added to the vertex flow by substituting $S \rightarrow \hat{G}$. This “Katanin substitution” [17], labeled by $1\ell_K$ in the following, was argued to yield a better fulfillment of WIs. A further refinement, which effectively incorporates the three-particle vertex to third order in the renormalized interaction, is obtained by the two-loop (2ℓ) vertex corrections [17,63,64].

Subsequently, the mfRG extension [9,15,16] was introduced to incorporate all those contributions of $\Gamma^{(6)}$ to the flow of Σ and F ensuring that their right-hand sides are *total* scale derivatives—which is not the case for the 1ℓ flow—thus guaranteeing by construction that the final results are independent of the choice of cutoff. In fact, the corresponding higher-loop terms of the mfRG represent the *minimal* additions to the conventional 1ℓ flow required to obtain cutoff-independent results. They also provide the *maximal* amount of diagrammatic contributions that can be added in a numerically feasible manner. Indeed, due to the iterative structure based on successive 1ℓ computations, these higher-loop contributions can be computed very efficiently [36]. Besides the two-dimensional Hubbard model [37], recent applications also include spin models [65,66] within the pseudofermion representation.

The mfRG was shown to formally reproduce the diagrammatic resummation of the PA. We use the vertex decomposition

$$F = R_{2\text{PI}} + \sum_r \gamma_r, \quad (5)$$

where γ_r are the two-particle reducible vertices in channel $r \in \{a, p, t\}$ and $R_{2\text{PI}}$ the fully two-particle irreducible (2PI) vertex (notation as in Ref. [9], cf. [67]). The PA then corresponds to the approximation $R_{2\text{PI}} = F_0$. An analogous approximation is performed in truncated fRG flows: Neglecting $\Gamma^{(6)}$, the vertex flow equation is of the form $\dot{F} = \sum_r \dot{\gamma}_r$. Thus, only the reducible parts are renormalized, while the fully irreducible part does not flow and remains at its initial value $R_{2\text{PI}} = F_0$.

In the following, we recall the flow equations for the self-energy, two-particle vertex, and susceptibilities, as well as the parquet equations. We will use the compact symbolic notation introduced in Ref. [9]; the explicit dependence on spin and frequencies will be given where needed.

One-loop flow—The “standard” fRG self-energy flow [10] is

$$\dot{\Sigma}_{\text{std}} = -F \cdot S, \quad (6)$$



FIG. 2. Diagrammatic representation of the multiloop flow of the susceptibility in the a channel. The doubly slashed lines denote $\dot{\Pi}_a$.

as illustrated in Fig. 1(a). Figure 1(b) shows an exemplary depiction of the 1ℓ flow of the vertices, given by

$$\dot{\gamma}_r^{(1)} = F \circ \dot{\Pi}_{r,S} \circ F, \quad (7)$$

and $\dot{F} = \sum_r \dot{\gamma}_r$. $\dot{\Pi}_{r,S}$ corresponds to the differentiated two-particle propagator in channel r , with S used instead of \dot{G} .

The flow equation for the susceptibilities χ_r can be derived from the corresponding reducible vertex in the limit of large fermionic frequencies, i.e., the so-called K_1 contribution [6],

$$\dot{\chi}_r^{(1)} = -\lambda_r \circ \dot{\Pi}_{r,S} \circ \lambda_r, \quad (8)$$

where λ_r are the renormalized three-point vertices (for further details and the 1ℓ flow equation of the latter, see Ref. [10]).

The $1\ell_K$ flow with Katanin substitution is obtained by replacing $S \rightarrow \dot{G}$, i.e., $\dot{\Pi}_{r,S} \rightarrow \dot{\Pi}_r$, in Eqs. (7) and (8). Since it includes self-energy (and not vertex) corrections from $\Gamma^{(6)}$, we will display the $1\ell_K$ results between those for $\ell=1$ and $\ell=2$.

Multiloop flow—The multiloop flow further includes the contributions from $\Gamma^{(6)}$, which are generated by vertex corrections. These can be ordered by loops, leading to the expansion $\dot{\gamma}_r = \sum_{\ell \geq 1} \dot{\gamma}_r^{(\ell)}$ [15,16]. Here, $\dot{\gamma}_r^{(1)}$ already includes the Katanin substitution to account for the self-energy corrections as above. The higher-loop terms, $\ell > 1$, are determined by

$$\dot{\gamma}_r^{(\ell)} = \dot{\gamma}_r^{(\ell-1)} \circ \Pi_r \circ F + F \circ \Pi_r \circ \dot{\gamma}_r^{(\ell-1)} \quad (\ell \geq 2) \quad (9a)$$

$$+ F \circ \Pi_r \circ \dot{\gamma}_r^{(\ell-2)} \circ \Pi_r \circ F \quad (\ell \geq 3), \quad (9b)$$

where $\gamma_{\bar{r}} = \sum_{r' \neq r} \gamma_{r'}$. Equation (9a) with $\ell=2$ corresponds to the 2ℓ flow, while the so-called center part $\dot{\gamma}_{r,C}^{(\ell)} = F \circ \Pi_r \circ \dot{\gamma}_r^{(\ell-2)} \circ \Pi_r \circ F$ of Eq. (9b) contributes only for $\ell \geq 3$.

In order to fully generate all parquet diagrams, the self-energy flow also acquires a multiloop correction [15],

$$\dot{\Sigma} = \dot{\Sigma}_{\text{std}} + (1 + F \circ \Pi_t) \circ \dot{\gamma}_{t,C} \cdot G, \quad (10)$$

where $\dot{\gamma}_{t,C} = \sum_{\ell \geq 3} \dot{\gamma}_{t,C}^{(\ell)}$ (see above). While not relevant for our AIM study, we note that additional approximations, such as the low-order expansion in form factors for the momentum-dependence of the vertex functions, useful for reducing the numerical effort in treating lattice problems, require extra adaptations of the flow equations for the mfRG solution to converge to the PA [37,68].

The multiloop flow equation for the susceptibilities reads

$$\dot{\chi}_r = -\lambda_r \circ (\dot{\Pi}_r + \Pi_r \circ \dot{I}_r \circ \Pi_r) \circ \lambda_r, \quad (11)$$

with the scale derivative of the two-particle irreducible vertex $\dot{I}_r = \sum_{\ell \geq 1} \dot{\gamma}_r^{(\ell)}$, see Fig. 2 for an exemplary diagrammatic representation. For more details and the equations for λ_r , we refer to Refs. [9,36].

PA—In parquet approaches [1], a set of self-consistent equations for the self-energy and vertex is solved by iteration. First, Σ is related to F by the Schwinger-Dyson

equation (SDE)

$$\Sigma = -F_0 \cdot G - \frac{1}{2}(F_0 \circ \Pi_a \circ F) \cdot G. \quad (12)$$

Second, in the decomposition (5), the two-particle reducible vertices γ_r are related to two-particle irreducible vertices I_r by the Bethe-Salpeter equations (BSEs)

$$\gamma_r = I_r \circ \Pi_r \circ F, \quad I_r = F - \gamma_r = R_{2\text{PI}} + \gamma_r. \quad (13)$$

In the PA, $R_{2\text{PI}} = F_0$. Finally, the susceptibilities χ_r can be directly deduced from F (and Σ via the propagators) by

$$\chi_r = -\lambda_{r,0} \circ (\Pi_r + \Pi_r \circ F \circ \Pi_r) \circ \lambda_{r,0}. \quad (14)$$

Here, $\lambda_{r,0}$ are the bare three-point vertices encoding the relation of the composite bosonic degrees of freedom of χ_r to the original fermionic ones.

In the parquet context, Eqs. (12)–(14) do not involve a scale parameter Λ . However, as they hold for any underlying bare propagator, they can also be applied when the bare propagator is G_0^Λ . These relations can then be used to derive the multi-loop flow equations [9], and thus Eqs. (12)–(14) are fulfilled exactly in mfRG [16,36]. In other truncated schemes, they can be exploited as additional *postprocessing* (PP) relations for computing (i) the self-energy from the SDE (12), (ii) the reducible vertices from the BSEs (13), and (iii) the susceptibilities using Eq. (14), instead of using the corresponding results of the flow. We recall that, for a generic truncated fRG scheme (including the standard 1ℓ truncation), the PP values of Σ , γ_r , and χ_r differ from their counterparts obtained directly from the flow. In fact, the equivalence between the flowing and PP results for Σ , γ_r , and χ_r (upon convergence) represents, besides the independence from the choice of the cutoff function, a hallmark of the mfRG [36]. For this reason, we will also compute the PP results for Σ and χ_r , and analyze their evolution with loop order.

QMC—Next to the fRG and PA described above, we use a state-of-the-art quantum Monte Carlo [39] (QMC) solver to obtain numerically exact benchmark results of the AIM. We employ continuous-time QMC in the hybridization expansion (CT-HYB) [39] provided by the open-access w2DYNAMICS [69] package. Further details on the calculations are provided in Appendix B 3.

III. mfRG SOLUTION OF THE AIM

We now apply the mfRG, briefly summarized in Sec. II, to the half-filled AIM at the inverse temperature $\beta = 10$ and discuss the results. For details on the implementation, we refer to Refs. [6,36]. We just note here that, for the reducible vertices, we adopt the parametrization $\gamma_r = K_{1r} + K_{2r} + K_{2'r} + K_{3r}$ proposed in Ref. [6]. The K_{1r} and $K_{2 \circ r}$ functions with one and two frequency arguments, respectively, describe the high-frequency asymptotics, while the remaining full dependence at low frequencies is contained in K_{3r} . This reduces the numerical cost, allowing for the calculation of the vertices on a larger Matsubara frequency range (see Appendix B 1 for computational details). The (flowing) susceptibilities are conveniently extracted through $\chi_r = -K_{1r}/U^2$.

We start the presentation of our numerical results by showcasing the central quantities of our study of the AIM, i.e., the self-energy Σ , the magnetic susceptibility $\chi_m (= -\chi_a^{\uparrow\downarrow})$, and

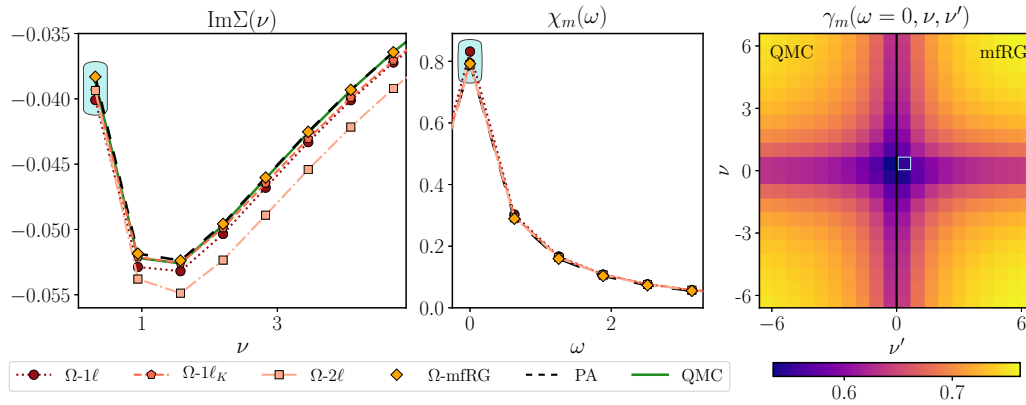


FIG. 3. Self-energy $\text{Im}\Sigma(\nu)$ (left), magnetic susceptibility $\chi_m(\omega)$ (center), and reducible vertex $\gamma_m = K_{1m} + K_{2m} + K_{2'm} + K_{3m}$ (right) as obtained by different approaches, for $U = 1$. We consider $\beta = 10$ and half filling throughout. The fRG results shown here are computed with the Ω flow [Eq. (3)]. The shaded areas in the first two panels and the frame in the right one mark the frequencies used to study the loop convergence in Secs. III A and III B.

the reducible vertex γ_m of the impurity site in the magnetic channel, computed in the weak-coupling regime ($U = 1$) by means of all the approaches mentioned in Sec. II. Figure 3 displays our results for Σ , χ_m , and γ_m as a function of fermionic (bosonic) Matsubara frequencies. The corresponding numerical data would also allow one to estimate important physical quantities (e.g., the quasiparticle mass renormalization and life time) relevant for the description of the Fermi-liquid state of the impurity problem [70,71] as well as to quantify the temporal fluctuations of the local magnetic moment on the impurity site [72–74].

Consistent with the small U value of these illustrative calculations, all approaches yield qualitatively the same behavior and deviations to numerically exact QMC data are hardly visible. In particular, we note that the converged mfRG solution (orange squares), perfectly matches the PA (dashed black line) for all quantities, $\text{Im}\Sigma$, χ_m , and γ_m (not shown). The results at the highlighted Matsubara frequencies are then used in the following Sec. III A for a quantitative study of the mfRG convergence as a function of loop order ℓ . There, we also showcase two hallmark qualities of the converged mfRG solution: (i) It is cutoff-independent, reflecting the fact that it reproduces the PA solution, which, as a self-consistent diagrammatic resummation, by construction is defined without reference to any cutoff. (ii) For quantities that can be computed either via their own RG flow equations or via PP relations, the results agree. (If the susceptibility flow is computed separately, and not via that of the K_{1r} part of the vertex, this requires to further use multiloop flow equations for the susceptibilities and the three-point vertices [9,36]). In Sec. III B, we extend this analysis to larger values of U .

A. Multiloop convergence to PA

In Fig. 4, we analyze in detail the loop convergence of the mfRG flow for $U = 1$. The four panels display both the flowing and PP results for $\text{Im}\Sigma(\nu = \pi T)$ and $\chi_m(\omega = 0)$ as well as the flowing results for $K_{2m}(\omega = 0, \nu = \pi T)$ and $K_{3m}(\omega = 0, \nu = \nu' = \pi T)$, as a function of loop order ℓ obtained with the two cutoffs, i.e., the Ω flow (red circles) and the U flow (blue

triangles). For comparison, the PA (black-dashed line) and QMC (green-solid line) solutions are also reported. One readily notices that the mfRG solution for *both* cutoffs converges to the PA for all considered quantities. Throughout the paper, the label “ ∞ ” refers to the infinite loop-order mfRG solution (see Appendix B 2 for its numerical definition). The high quality of the mfRG convergence can be appreciated by looking at the corresponding insets, showing the data restricted to higher loop orders. While the gray area in the main panels marks 1% deviation with respect to the PA, the blue area in the insets corresponds to 0.1%.

It is worth stressing that for some quantities and specific values of ℓ , the mfRG and PA solution may be accidentally close, e.g., the 3ℓ Ω -flow result for $\chi_m(\omega = 0)$ or the 3ℓ U -flow result for $K_{3m}(\omega = 0, \nu = \nu' = \pi T)$. Of course, this does not mean that the mfRG procedure has already converged at 3ℓ : Full convergence implies the equivalence of mfRG and PA for *all* quantities and *both* cutoffs up to differences smaller than a given ϵ , e.g., here 0.1%. For the $U = 1$ calculations, this is clearly achieved for $\ell \geq 8$. Looking at the insets, the Ω flow appears to converge systematically faster than the U flow. We note that all U -flow results shown in the paper are obtained via a frequency extrapolation (see Appendix B 1), which is required to achieve the highly precise convergence to PA demonstrated in the inset.

Another important property of the converged mfRG solution is the equivalence of the flowing and PP results, shown both for $\text{Im}\Sigma(\nu = \pi T)$ and $\chi_m(\omega = 0)$ in the upper panels of Fig. 4. Except for the 1ℓ and $1\ell_K$ results for the self-energy, the PP data (dotted lines with “ \times ” or “ $+$ ” symbols) are always found to be closer to the PA than the flowing data (for the susceptibility, this trend was previously reported in Ref. [37]). For both cutoffs, flowing and PP results agree with the PA for $\ell \geq 8$, highlighting the perfect convergence of the mfRG scheme in this parameter regime. The loop convergence can also be seen from calculations with a single cutoff, as there are no more changes larger than a small ϵ in all quantities when going from ℓ to $\ell + 1$, and flowing and PP results agree with one another. Finally, let us note that adopting the PP procedure has also important implications for the fulfillment of sum rules, which are studied in Sec. IV A.

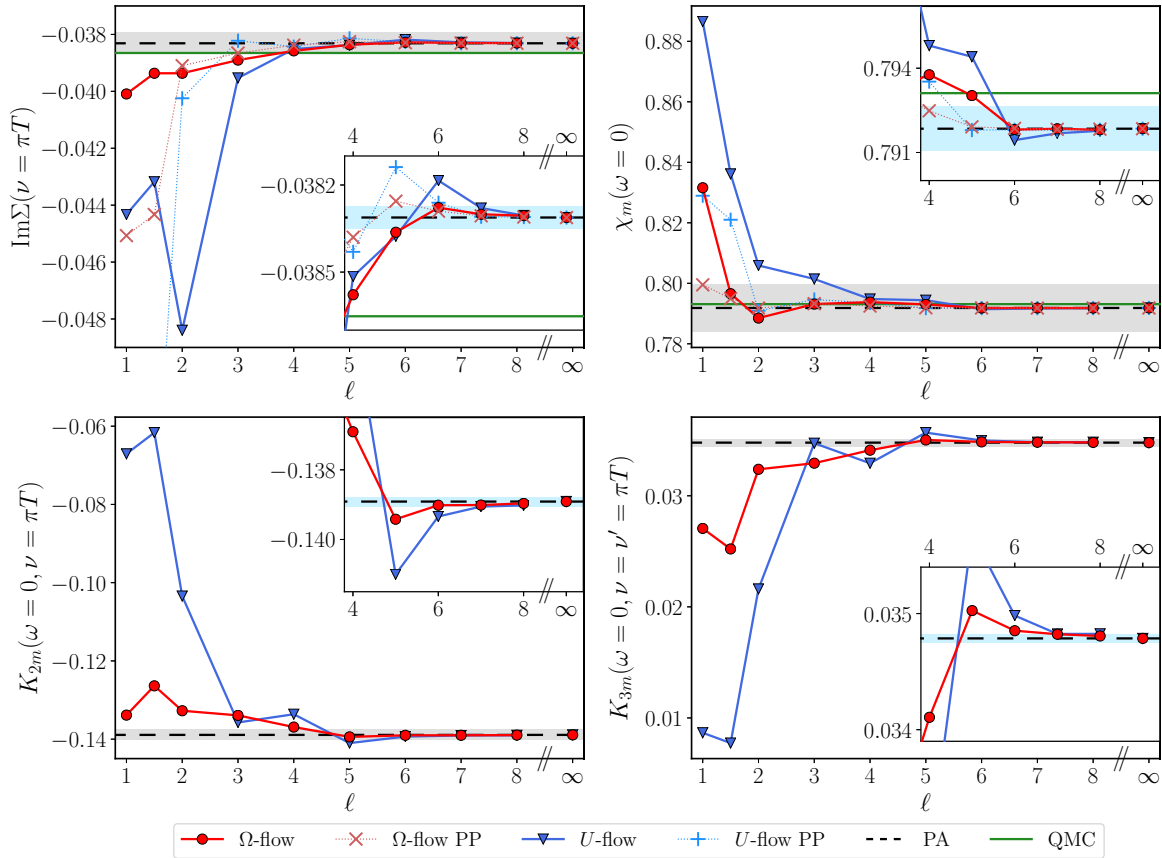


FIG. 4. Ω -flow (red) and U -flow (blue) mFRG results as a function of loop order ℓ in comparison with the PA (black, dashed) and the numerically exact QMC data (green), for $U = 1$. Upper panels: $\text{Im}\Sigma(\nu = \pi T)$ and $\chi_m(\omega = 0)$, showing perfect agreement between post-processed (PP) and flowing results of both cutoffs and the PA result. Lower panels: Asymptotic vertex functions K_{2m} and K_{3m} for the lowest Matsubara frequencies. Insets show a zoom for $\ell \geq 4$. The gray areas mark 1% deviation from the PA result, the blue ones in the insets 0.1%. The label “ ∞ ” represents the fully converged mFRG result. In this and similar figures below, the data points plotted between those at $\ell = 1$ and $\ell = 2$ represent the $1\ell_K$ results (Katanin substitution).

B. Towards strong coupling

We now analyze how the convergence of the mFRG flow is affected by increasing the interaction U . In Figs. 5–7, we focus on the results for the physical quantities $\text{Im}\Sigma(\nu = \pi T)$ and

$\chi_m(\omega = 0)$, but we also checked for convergence of $K_{2m}(\omega = 0, \nu = \pi T)$ and $K_{3m}(\omega = 0, \nu = \nu' = \pi T)$.

For values of U slightly larger than $U = 1$, the convergence behavior is qualitatively the same (see Fig. 17 in Appendix A

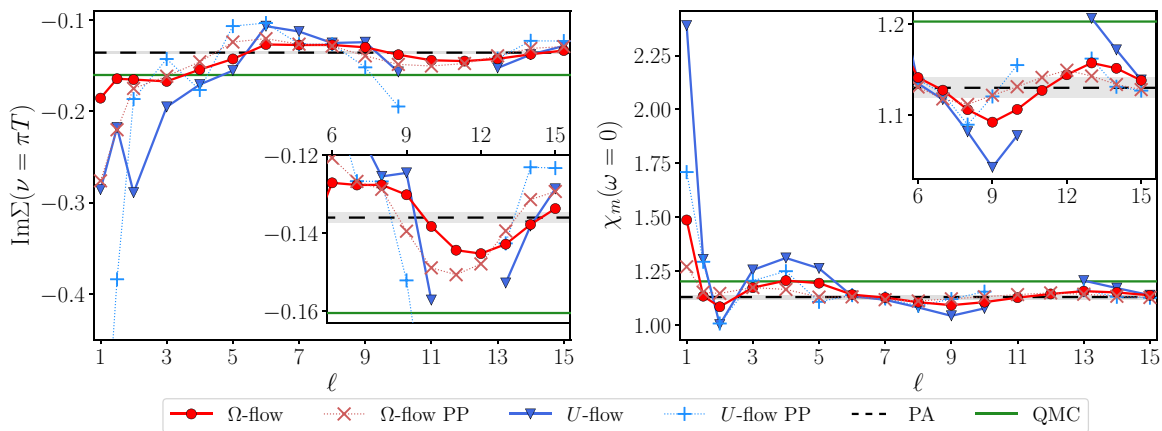


FIG. 5. $\text{Im}\Sigma(\nu = \pi T)$ and $\chi_m(\omega = 0)$ as in Fig. 4 but for $U = 2$. Insets show a zoom for $\ell \geq 6$. The gray area indicates 1% deviation from the PA. For $\ell = 11, 12$ we were unable to converge the U -flow calculations.

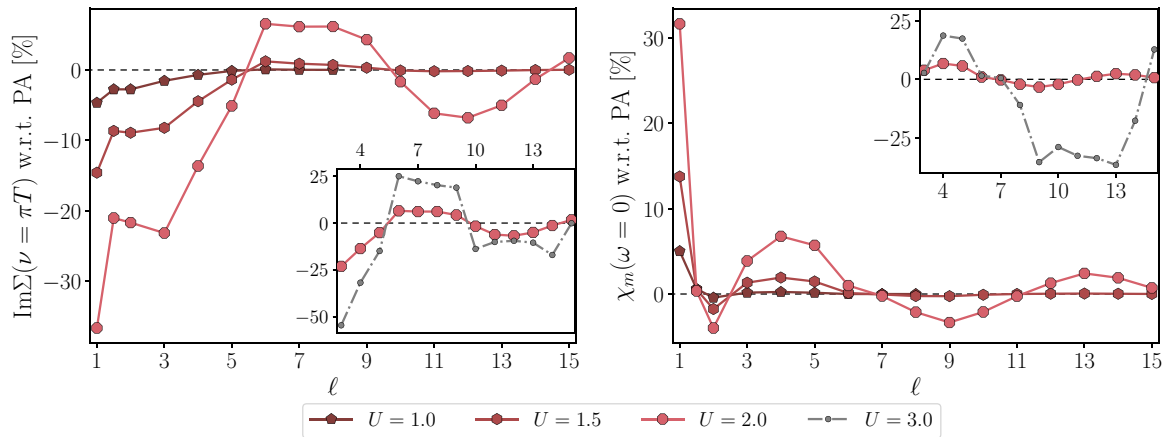


FIG. 6. Relative difference between Ω -flow mFRG calculations (flowing) and the corresponding PA solutions for $\text{Im}\Sigma(\nu = \pi T)$ (left) and $\chi_m(\omega = 0)$ (right), as a function of loop order ℓ and different values of the interaction U . Main panels show $U \leq 2$, insets $U \geq 2$.

for $U = 1.5$), albeit with increasing interaction, as expected, more loop orders are required to reach convergence.

For $U = 2$, the dependence on loop order is shown in Fig. 5. While the mFRG solution quickly approaches the PA for low ℓ , the path towards full convergence for higher ℓ

becomes visibly slower as the curves describing the loop dependence of the mFRG calculations keep oscillating around the PA solution. The Ω -flow results are generally found to be more accurate than the U -flow data (note that for the U flow at $\ell = 11, 12$, no solution could be obtained; see also Appendix B 2). Yet, even with the Ω flow, we did not reach perfect convergence up to $\ell = 40$. Different from the situation at $U = 1$ and $U = 1.5$, the results obtained by PP do not show a clear improvement. Instead, they seem to follow a slightly different oscillation pattern, somewhat shifted from the flowing data (see insets of Fig. 5). Further insight on the oscillations characterizing the mFRG convergence with increasing interaction can be gained from Fig. 6. Here, we show the relative difference between the mFRG results and the corresponding PA solutions for different values of U . By comparing the (flowing) results of the Ω flow for different interaction strengths $U = 1, 1.5$, and 2 , one notices the presence of “nodes” in the multiloop oscillations, i.e., of loop orders at which mFRG and PA yield numerically very similar results for the quantity under consideration. The location of these nodes, however, depends on the observable. [While, e.g., $\ell = 7$ for $\chi_m(\omega = 0)$ is close to the PA for all values of U , for $\text{Im}\Sigma(\nu = \pi T)$ this is not the case.] For larger interactions, the oscillations become stronger. Already for $U = 2$, the amplitude of the self-energy oscillations hardly decreases with increasing loop order, making a full convergence numerically challenging as discussed above. (The U flow shows similar behavior, see Fig. 18 in Appendix A). This effect gets even more pronounced for $U = 3$ displayed in the insets, together with $U = 2$ for comparison. There, higher loop orders, especially for $\chi_m(\omega = 0)$, yield a progressively enhanced deviation from the PA for increasing loop order. Therefore, we conclude that, within our current implementation and the given settings of the AIM, the mFRG loop resummation ceases to converge for $U = 3$. Such a lack of loop convergence serves as a built-in red-flag indicator that a parameter regime lies outside the zone of safe applicability of the approach. This outcome, however, is not entirely unexpected since, for the specific AIM considered, the interaction strength $U = 3$ already corresponds to the strong-coupling regime, where nonperturbative [51,75–77] divergences of two-particle irreducible vertices [78–85], which are—per construction—beyond the PA, were detected

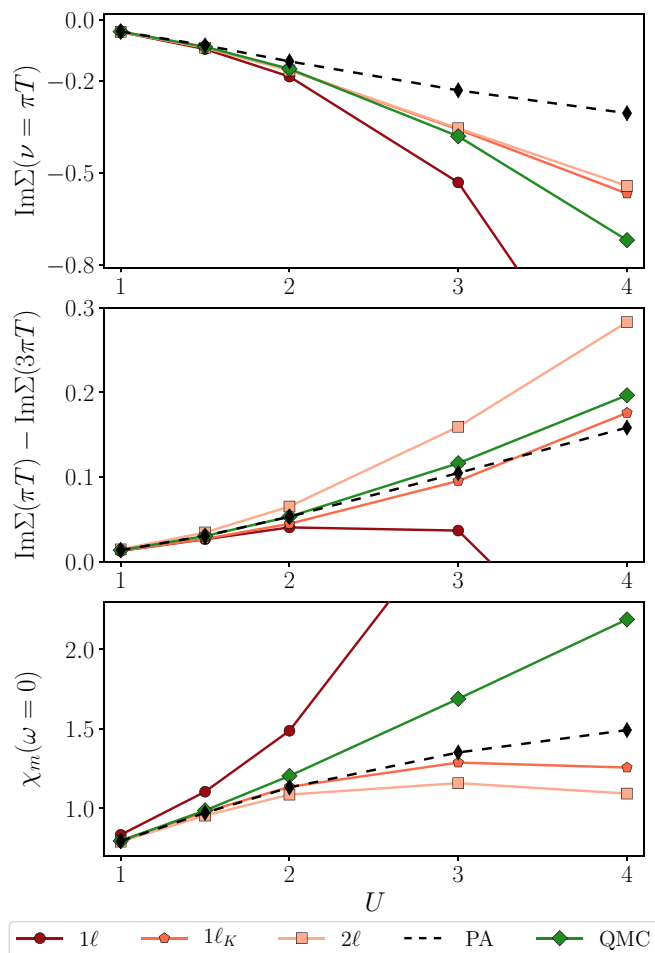


FIG. 7. $\text{Im}\Sigma(\pi T)$ (top), $\text{Im}\Sigma(\pi T) - \text{Im}\Sigma(3\pi T)$ (center), and $\chi_m(\omega = 0)$ (bottom) as a function of U , obtained from Ω flows at low loop order, the PA, and QMC.

by means of QMC calculations [51,60]. More speculatively, one might then suppose a relation between the breakdown of the mfRG convergence and the entrance into the nonperturbative parameter regime, where the PA itself yields results significantly different from the exact solution [51]. In this respect, the oscillations of increasing size could be seen as a precursor of the breakdown of perturbative resummation schemes.

We finally compare the results of low loop orders to the PA and the exact solution, as a function of U . For very low values of U , the deviations of mfRG and PA schemes from QMC can be qualitatively understood from general perturbation-theory considerations. Already for $U > 1$, however, the interpretation becomes more complicated, and the accuracy of the different schemes depends on the observable considered. Among the Ω -flow results up to $U = 4$ in Fig. 7, the plain 1ℓ flow performs worst for all quantities. Comparing $1\ell_K$ and the PA to the exact QMC for large $U \geq 2$, we find the best results for $\text{Im}\Sigma(\nu = \pi T)$ with $1\ell_K$, similar deviations for $\text{Im}\Sigma(\nu = \pi T) - \text{Im}\Sigma(\nu = 3\pi T)$ with $1\ell_K$ and the PA, and the best results for $\chi_m(\omega = 0)$ with the PA. For the physical interpretation of the strong-coupling regime, we refer to Ref. [51] and the corresponding supplemental material. There it was shown that both the PA and fRG schemes yield a qualitatively correct description of the magnetic channel; in particular, the proper behavior of $\chi_m(\omega = 0)$ as a function of T is found, reflecting the formation of a local magnetic moment and its screening. However, both methods fail in describing the associated suppressed fluctuations in the charge sector, which are heavily affected by the emergence of the local magnetic moment. Hence, at strong coupling, the truncated fRG, mfRG, or PA resummations of diagrams describe the formation of a local moment without the intrinsic physical implications onto the charge channel. This can be regarded [51,86] as an insufficient transfer of information between the magnetic and the charge sector, formally corresponding to the impossibility of generating the irreducible vertex divergences in these approximate methods.

On a more general perspective, we note that the loop convergence of the mfRG procedure is mostly controlled by the ratio between the local interaction U and other relevant energy scales of the system under consideration (e.g., in the case of the AIM: $\pi\Delta$ or the temperature T) rather than by the ratio between the temperature and the Kondo temperature [51]. In future dedicated studies, it may be interesting to verify to what extent the grade of the loop convergence itself might be regarded as an additional independent marker of central physical aspects of the underlying exact solution of the problem.

IV. PAULI PRINCIPLE AND WARD IDENTITY

Both the Pauli principle and the WIs are fundamental features of the many-electron physics. They are deeply rooted in quantum mechanics and pose important constraints on many-body correlation functions. An exact solution must evidently obey all such constraints. In approximate treatments, however, their fulfillment is not guaranteed *a priori*. As mentioned in the Introduction, it is commonly reckoned [1] that approximate many-body approaches either obey sum rules imposed by the Pauli principle *or* satisfy WIs. Hence, fulfilling both

the Pauli principle and the WIs would represent a specific hallmark of the exact solution. On a more formal level, a pertinent example of such a trade-off in the context of parquet-based approximations can be obtained by exploiting explicit relations between the self-energy and four-point vertices [7–9] in the parquet formalism.

In the following, we utilize our converged numerical results for the AIM to analyze, on a quantitative level, to what extent the Pauli principle and WIs are fulfilled for the important class of approximate many-body approaches ranging from the conventional fRG to the mfRG and PA.

A. Pauli principle

Sum rule of $\chi^{\sigma\sigma}$: Formal aspects—The Pauli exclusion principle states that two electrons cannot occupy the same quantum state. On the operator level, this corresponds to the fact that a fermionic occupation-number operator can only have eigenvalues zero and one. On the diagrammatic level, such a constraint affects the many-body correlation functions in several ways, e.g., through sum rules they must obey.

In this context, a relevant correlation function for the physics of the AIM is the equal-spin density-density susceptibility,

$$\chi^{\sigma\sigma}(\tau) = \langle T_\tau \hat{n}_\sigma(\tau) \hat{n}_\sigma \rangle - n_\sigma^2. \quad (15)$$

Here, $n_\sigma = \langle \hat{n}_\sigma \rangle$, and T_τ denotes (imaginary) time ordering (for brevity, we omit here the particle-hole channel label). This susceptibility is directly affected by the Pauli principle through the operator identity $\hat{n}_\sigma^2 = \hat{n}_\sigma$. Indeed, an evaluation at $\tau = 0$ yields

$$\chi^{\sigma\sigma}(\tau = 0) = \langle \hat{n}_\sigma^2 \rangle - n_\sigma^2 = n_\sigma(1 - n_\sigma), \quad (16)$$

a value, which is fully determined by the single-particle expectation value n_σ . Furthermore, as the equal-time correlator $\chi^{\sigma\sigma}(\tau = 0)$ is identical to the sum over all its Fourier components $\chi_\omega^{\sigma\sigma}$, the following sum rule [87] must hold:

$$\frac{1}{\beta} \sum_\omega \chi_\omega^{\sigma\sigma} = \chi^{\sigma\sigma}(\tau = 0) = n_\sigma(1 - n_\sigma). \quad (17)$$

At SU(2) spin symmetry and half filling, the result is 1/4.

For the purposes of the subsequent discussions, it is useful to elaborate on the quantum-field-theoretical relations which underlie Eq. (17). To this end, we recall that the Pauli principle can be translated from an operator identity ($\{\hat{d}_\sigma, \hat{d}_{\sigma'}\} = 0$, $\{\hat{d}_\sigma, \hat{d}_\sigma^\dagger\} = \delta_{\sigma\sigma'}$) to the crossing symmetry of four-point correlators. For illustration, let us briefly use a compact notation where all arguments of an electronic operator are summarized in a single index. Then, for $G_{1,2;1',2'}^{(4)} \propto \langle T_\tau d_1 d_2 d_1^\dagger d_2^\dagger \rangle$, the crossing symmetry implies $G_{1,2;1',2'}^{(4)} = -G_{2,1;1',2'}^{(4)} = -G_{1,2;2',1'}^{(4)}$.

Furthermore, the susceptibility can be represented through (full) propagators G and the (full) two-particle vertex F by

$$\chi_\omega^{\sigma\sigma} = -\frac{1}{\beta} \sum_\nu G_{\nu+\omega}^\sigma G_\nu^\sigma - \frac{1}{\beta^2} \sum_{\nu\nu'} G_{\nu+\omega}^\sigma G_\nu^\sigma G_{\nu'+\omega}^\sigma G_{\nu'}^\sigma F_{\nu,\nu'+\omega;\nu',\nu+\omega}^{\sigma\sigma}, \quad (18)$$

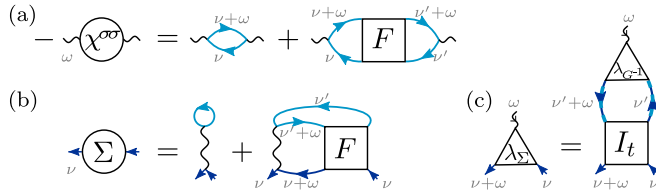


FIG. 8. Identities between many-body correlation functions. Dark and light colors on electron propagators distinguish the two spins. Frequency labels are given for clarity. (a) The susceptibility $\chi^{\sigma\sigma}$ consists of a bubble term and corrections in terms of the full vertex F , see Eq. (18). (b) SDE (26) for the self-energy Σ , consisting of the static Hartree part and additions containing F . (c) The WI of Eq. (30) relating Σ to I_t , the vertex irreducible in the transverse (vertical) particle-hole channel. Dashed dark and light colors indicate a sum over spin. Triangles represent objects defined in Eqs. (29) and (30).

as illustrated in Fig. 8(a). The first term of Eq. (18) summed over all frequencies ω , i.e., taken at $\tau = 0$, gives

$$\chi_{GG}^{\sigma\sigma}(\tau = 0) = -G^\sigma(\tau = 0^-)G^\sigma(\tau = 0^+). \quad (19)$$

Upon inserting $G^\sigma(\tau) = -(T_\tau \hat{d}(\tau) \hat{d}^\dagger)$, one finds

$$\chi_{GG}^{\sigma\sigma}(\tau = 0) = \langle d_\sigma^\dagger d_\sigma \rangle \langle d_\sigma d_\sigma^\dagger \rangle = n_\sigma(1 - n_\sigma), \quad (20)$$

which yields already the *entire* sum rule [Eq. (17)]. Consequently, the vertex contributions must vanish when summed over all frequencies ω . This is indeed guaranteed by the crossing symmetry, as we show below.

Consider the summed vertex contribution of Eq. (18),

$$\frac{1}{\beta} \sum_{\omega} \chi_{\text{vtx};\omega}^{\sigma\sigma} = -\frac{1}{\beta^3} \sum_{\omega\nu\nu'} G_{\nu+\omega}^\sigma G_\nu^\sigma G_{\nu'+\omega}^\sigma G_{\nu'}^\sigma F_{\nu,\nu'+\omega;\nu+\omega,\nu'}^{\sigma\sigma}. \quad (21)$$

For $F^{\sigma\sigma}$, the vertex with equal spins on all legs, the crossing symmetry simply gives $F_{\nu'_1,\nu'_2;\nu_1,\nu_2}^{\sigma\sigma} = -F_{\nu'_1,\nu'_2;\nu_2,\nu_1}^{\sigma\sigma}$. After inserting this into Eq. (21), we relabel the summation indices according to $\tilde{\omega} = \nu' - \nu$, $\tilde{\nu} = \nu + \omega$:

$$\begin{aligned} \frac{1}{\beta} \sum_{\omega} \chi_{\text{vtx};\omega}^{\sigma\sigma} &= \frac{1}{\beta^3} \sum_{\omega\nu\nu'} G_{\nu+\omega}^\sigma G_\nu^\sigma G_{\nu'+\omega}^\sigma G_{\nu'}^\sigma F_{\nu,\nu'+\omega;\nu+\omega,\nu'}^{\sigma\sigma} \\ &= \frac{1}{\beta^3} \sum_{\tilde{\omega}\tilde{\nu}} G_{\tilde{\nu}}^\sigma G_{\tilde{\nu}}^\sigma G_{\tilde{\omega}+\tilde{\nu}}^\sigma G_{\tilde{\omega}+\tilde{\nu}}^\sigma F_{\nu,\tilde{\omega}+\tilde{\nu};\tilde{\nu},\tilde{\omega}+\tilde{\nu}}^{\sigma\sigma}. \end{aligned} \quad (22)$$

This reproduces the original expression for the summed vertex correction $\frac{1}{\beta} \sum_{\omega} \chi_{\text{vtx};\omega}^{\sigma\sigma}$ [Eq. (21)] with opposite sign, so that

$$\frac{1}{\beta} \sum_{\omega} \chi_{\text{vtx};\omega}^{\sigma\sigma} = -\frac{1}{\beta} \sum_{\omega} \chi_{\text{vtx};\omega}^{\sigma\sigma} \Rightarrow \frac{1}{\beta} \sum_{\omega} \chi_{\text{vtx};\omega}^{\sigma\sigma} = 0. \quad (23)$$

Sum rule of $\chi^{\sigma\sigma}$: Numerical results—As mentioned in Sec. II, there are two ways [10,36] of computing susceptibilities in fRG: (i) one can use Eq. (18) to obtain χ from Σ and F in a PP fashion, or (ii) one can deduce χ from its own flow equation. In the former approach the sum rule of $\chi^{\sigma\sigma}$ is fulfilled per construction, as long as the vertex used in the computation obeys the crossing symmetry, see Eqs. (20) and (23), while, in the latter scheme, this property is not guaranteed.

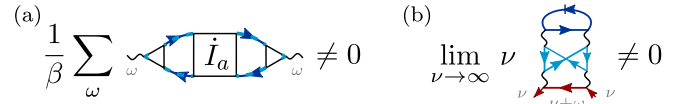


FIG. 9. (a) The multiloop corrections to the flow of $\chi^{\sigma\sigma}$ do not vanish when summed over ω , since I_a itself is not crossing symmetric. (b) Totally irreducible “envelope” vertex diagrams inserted into the standard self-energy flow contribute to the $1/\nu$ asymptote of Σ . Red colors indicate propagators that carry the large frequency ν .

Not surprisingly, strategies (i) and (ii) then yield different results within 1ℓ fRG (see Figs. 4 and 5), suggesting that the susceptibility computed from a 1ℓ flow does not fulfill the sum rule. Indeed, one can easily convince oneself that the multiloop vertex corrections to the flow of $\chi^{\sigma\sigma}$ do not vanish when summing over all frequencies, cf. Fig. 9(a). On the other hand, we already noted that, for a converged mfRG calculation, both schemes of computing susceptibilities become equivalent [9,36]. Therefore, the sum rule of $\chi^{\sigma\sigma}$ will be consistently fulfilled, no matter the strategy employed.

On the basis of these considerations, we now turn to our numerical mfRG data. In Fig. 10, we show the loop dependence of $\frac{1}{\beta} \sum_{\omega} \chi_{\omega}^{\sigma\sigma}$ for the flowing susceptibility (obtained in the Ω flow) for different values of U . With increasing loop order, the fulfillment of the sum rule [Eq. (17)], indicated by a dashed-black line, is approached. Altogether, we observe a similar behavior as in Sec. III: While, at low interaction values, the exact value is quickly reached, multiloop oscillations characterize the behavior at larger interaction ($U=2$). Nevertheless, even for large U , the results at large ℓ are much closer to the fulfillment of the sum rule than the ones at low loop order. As for the PP susceptibility (not shown), we confirmed numerically that it fulfills the sum rule for all ℓ , consistent with the above explanations.

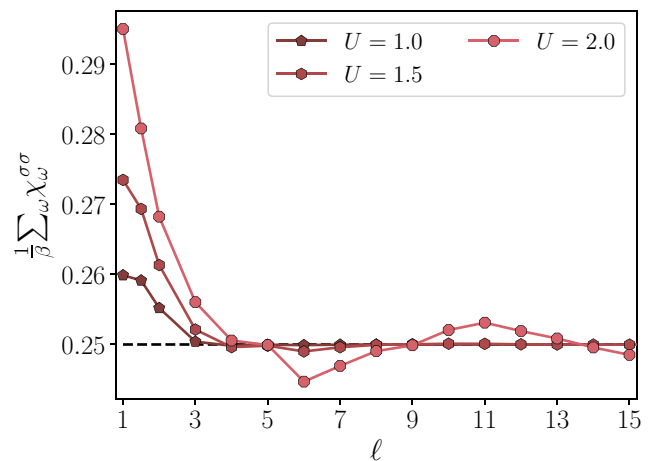


FIG. 10. The frequency sum of $\chi_{\omega}^{\sigma\sigma}$ obtained for different values of U and loop order ℓ (in the Ω flow). The multiloop corrections systematically improve the fulfillment of the sum rule [Eq. (17)]. Upon multiloop convergence, the sum rule is exactly fulfilled, as in the PA (dashed-black line).

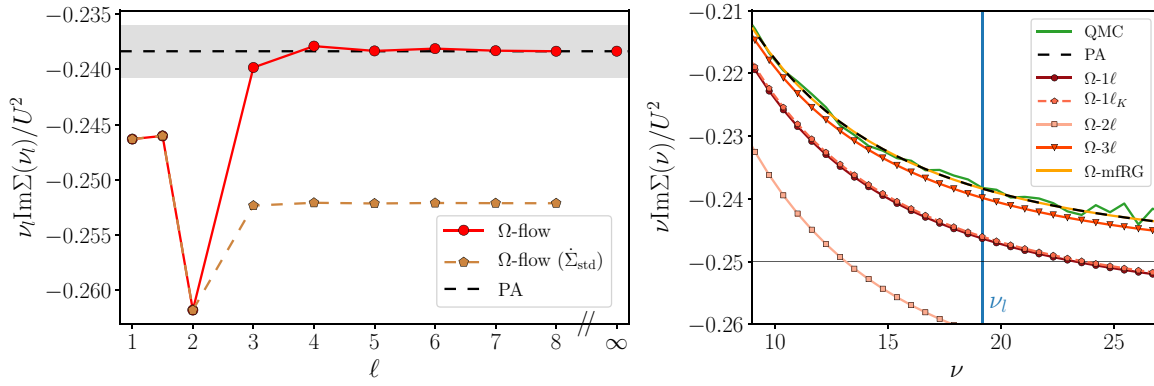


FIG. 11. High-frequency asymptote of the self-energy, $\nu_l \text{Im} \Sigma(\nu_l)/U^2$, for a large but finite frequency $\nu_l \approx 19.16$ ($\nu_l \text{Im} \Sigma(\nu_l)/U^2 \rightarrow -\frac{1}{4}$ for $\nu_l \rightarrow \infty$), for $U=1$. Left: Flowing result as a function of loop order, for an Ω flow with (red circles) and without (gold pentagons) multiloop corrections to the self-energy flow, compared to the PA (black dashed). The gray area represents 1% deviation from PA. Right: Frequency dependence around ν_l for different methods, with QMC, PA, and mfRG following the exact asymptote.

High-frequency asymptote of Σ : Formal aspects—Beside its natural link to the density susceptibility, the Pauli principle also affects the self-energy, albeit more indirectly. From the moments of the single-particle spectral function, known through expectation values of operators, one can determine the high-frequency expansion of the propagator G , and thereby of the self-energy Σ [87]. One finds

$$\Sigma_v^\sigma = U n_{\bar{\sigma}} + \frac{U^2 n_{\bar{\sigma}} (1 - n_{\bar{\sigma}})}{i\nu} + O\left(\frac{1}{\nu^2}\right). \quad (24)$$

Next to the constant Hartree shift $U n_{\bar{\sigma}}$, the $1/\nu$ coefficient coincides with the right-hand side (r.h.s.) of the sum rule for $\chi^{\bar{\sigma}\bar{\sigma}}$ [Eq. (17)]. Indeed, Eq. (24) can be equivalently rewritten [88] as

$$\Sigma_v^\sigma = U n_{\bar{\sigma}} + \frac{U^2}{i\nu} \frac{1}{\beta} \sum_{\omega} \chi_{\omega}^{\bar{\sigma}\bar{\sigma}} + O\left(\frac{1}{\nu^2}\right). \quad (25)$$

More insight about the quantum-field-theoretical relations underlying the asymptotic behavior of Σ can be gained from the SDE,

$$\Sigma_v^\sigma = U n_{\bar{\sigma}} + \frac{U}{\beta^2} \sum_{\omega, \nu'} G_{v+\omega}^\sigma G_{v'+\omega}^{\bar{\sigma}} G_{\nu'}^{\bar{\sigma}} F_{v'+\omega, \nu; v+\omega, \nu'}^{\sigma\bar{\sigma}}, \quad (26)$$

see Fig. 8(b). To this end, let us replace the vertex by its bare contribution, $F_0^{\sigma\bar{\sigma}} = -U$, and use the first propagator in Eq. (26), $G_{v+\omega}^\sigma$, to factor out the dominant contribution for large $\nu \gg \omega$, $G_{v+\omega}^\sigma \sim 1/(i\nu)$. The remainder is a GG bubble summed over both frequencies ω and ν' . Hence, we find that the second-order contribution,

$$\Sigma_v^\sigma \stackrel{\text{2nd}}{\sim} \frac{-U^2}{i\nu} G^{\bar{\sigma}}(\tau=0^-) G^{\bar{\sigma}}(\tau=0^+) = \frac{U^2 n_{\bar{\sigma}} (1 - n_{\bar{\sigma}})}{i\nu}, \quad (27)$$

already provides the correct asymptotic behavior (24). This is similar to the sum rule of $\chi^{\sigma\sigma}$, where Eqs. (19)–(20) give the entire result, while the summed vertex corrections vanish [Eq. (23)]. Via Eq. (25), the same cancellation of vertex corrections occurs for the self-energy asymptote, as we explicitly show in Appendix C 1.

Within an fRG treatment, the standard flow equation for the self-energy $\tilde{\Sigma}_{\text{std}}$ in terms of the vertex F is *in principle*

exact, as long as the exact vertex F is available. As this is almost never the case, the flow $\tilde{\Sigma}_{\text{std}}$ must be considered approximate. In mfRG, the multiloop corrections to the self-energy flow [cf. Eq. (10)] effectively generate contributions to $\tilde{\Sigma}_{\text{std}}$, which *would* require—when using the term $\tilde{\Sigma}_{\text{std}}$ only—vertex diagrams beyond the PA (and thus beyond 1ℓ fRG). Indeed, one can generally show that vertex diagrams beyond the PA (and thus beyond 1ℓ fRG), such as the envelope diagram, do contribute to $\tilde{\Sigma}_{\text{std}}$ to order $1/\nu$ in the large-frequency limit [cf. Fig. 9(b)]. Therefore, the Σ asymptote [Eq. (24)] is violated when using a 1ℓ or multiloop vertex flow while keeping the standard self-energy flow. This problem is circumvented by including the multiloop corrections to the self-energy flow [16], which guarantee a perfect equivalence to the SDE and, thereby, that the correct asymptote will be restored.

High-frequency asymptote of Σ : Numerical results—In Fig. 11, we show (flowing) results for the asymptotic behavior of Σ as obtained from Ω -flow calculations for $U=1$. The left panel displays $\nu \text{Im} \Sigma_v/U$ as a function of ℓ for a fixed, large value of $\nu_l \approx 19.16$. At this frequency, $\nu \text{Im} \Sigma_v$ is expected to be slightly lower (in absolute value) than the corresponding asymptotic value of $-1/4$ for $\nu \rightarrow \infty$. The correct asymptotic description of the mfRG results (red circles) for large ℓ is demonstrated by their perfect match with the corresponding PA results, as the latter yield the correct high-frequency asymptotic by construction. As explained above, this would have not been the case without multiloop corrections to the self-energy flow. In fact, the gold pentagon line shows results, which are obtained by $\tilde{\Sigma}_{\text{std}}$ without multiloop additions to the self-energy flow (these start at $\ell=3$) and notably deviate from the correct value.

The right panel shows the frequency dependence of $\nu \text{Im} \Sigma_v$ in a frequency window around ν_l (ν_l is represented by the vertical blue line). For fRG results at lower loop order, the high-frequency asymptote is incorrect, reflecting the fact that the SDE relation is not fulfilled. For the same reason, all approaches satisfying the SDE lie on top of each other, i.e., the PA (black-dashed line), mfRG (orange-solid line), and QMC (green line) [89] yield the correct high-frequency behavior of Σ . While the improvement of the high-frequency results

is not monotonous for the lowest loop orders, we observe that rather accurate results are obtained already at the 3ℓ level, where the first multiloop corrections to the self-energy flow appear. In this respect, it is also interesting to note that the standard self-energy flow $\tilde{\Sigma}_{\text{std}}$ provides a large-frequency asymptote in agreement with Eq. (25), but with $\chi^{\sigma\sigma}$ obtained by a one-loop flow and thus violating the sum rule [Eq. (17)]. We derive this result in Appendix C 1 and show explicitly which multiloop additions to $\tilde{\Sigma}_{\text{std}}$ contribute to the asymptote.

B. Ward identities

Formal aspects—The WIs play an essential role in the many-electron theory as they define how the information encoded in the continuity equations at a microscopical level is reflected onto response functions and macroscopic quantities. More specifically, a continuity equation is an operator relation of the form $\partial_\tau \hat{\rho} = -[\hat{\rho}, \hat{H}]$. If $\hat{\rho}$ is a symmetry of the Hamiltonian, $[\hat{\rho}, \hat{H}] = 0$, then $\hat{\rho}$ is a conserved quantity, $\partial_\tau \hat{\rho} = 0$. In this case, the continuity equation describes a conservation law. However, even if this is not the case, continuity relations can be used for deriving relevant WIs, in particular when $[\hat{\rho}, \hat{H}]$ —albeit nonzero—yields a simple expression.

In practice, WIs can be derived for n -point correlation functions of arbitrary n . If $\hat{\rho}$ and $[\hat{\rho}, \hat{H}]$ involve n_1 and $n_2 = n_1 + \delta n$ fermionic operators, respectively, then

$$\langle T_\tau \hat{c}_1 \cdots \hat{c}_{n-n_1}^\dagger \partial_\tau \hat{\rho} \rangle = -\langle T_\tau \hat{c}_1 \cdots \hat{c}_{n-n_1}^\dagger [\hat{\rho}, \hat{H}] \rangle \quad (28)$$

relates an n to an $(n + \delta n)$ -point function. Typically, one mostly considers the WI connecting two- and four-point functions (i.e., the WIs ensuring the physical consistency between the one- and the two-particle description) and restricts oneself to the (local or global) charge or spin operators, substituting them for $\hat{\rho}$. A recent derivation, applicable to lattice and impurity systems, as well as references to prior studies can be found in Refs. [90,91]. Here, we consider explicitly the (local) charge, $\hat{\rho} = \sum_\sigma \hat{n}_\sigma$, as done in several preceding papers [17,92]. The resulting WI for the AIM, formulated in a way that allows for an optional SU(2) spin symmetry breaking (e.g., by a Zeeman field), reads

$$\underbrace{\Sigma_{\nu+\omega}^\sigma - \Sigma_\nu^\sigma}_{\mathcal{W}_L} = -\frac{1}{\beta} \underbrace{\sum_{\sigma'\nu'} I_{t; \nu+\omega, \nu'; \nu, \nu'+\omega}^{\sigma\sigma'} (G_{\nu'+\omega}^{\sigma'} - G_{\nu'}^{\sigma'})}_{\mathcal{W}_R}. \quad (29)$$

We introduce the short-hand $\mathcal{W}_L(\nu, \omega)$ for the left and $\mathcal{W}_R(\nu, \omega)$ for the right side of the above equation, which is illustrated diagrammatically in Fig. 8(c). There, we use $\lambda_{\Sigma; \omega, \nu}^\sigma = \Sigma_{\nu+\omega}^\sigma - \Sigma_\nu^\sigma$ and $\lambda_{G^{-1}; \omega, \nu'}^{\sigma'} = (G_{\nu'+\omega}^{\sigma'})^{-1} - (G_{\nu'}^{\sigma'})^{-1}$, such that Eq. (29) becomes

$$\lambda_{\Sigma; \omega, \nu}^\sigma = \frac{1}{\beta} \sum_{\sigma'\nu'} I_{t; \nu+\omega, \nu'; \nu, \nu'+\omega}^{\sigma\sigma'} G_{\nu'+\omega}^{\sigma'} \lambda_{G^{-1}; \omega, \nu'}^{\sigma'}. \quad (30)$$

For our numerical results we exploit the SU(2) spin symmetry, which—together with the crossing symmetry—entails

$$I_{t; \nu_1', \nu_2'; \nu_1, \nu_2}^{\uparrow\uparrow} = I_{t; \nu_1', \nu_2'; \nu_1, \nu_2}^{\uparrow\downarrow} - I_{a; \nu_1', \nu_2'; \nu_2, \nu_1}^{\uparrow\downarrow}. \quad (31)$$

Eventually, we briefly recall that one often refers to *functional* WIs, such as $\frac{\delta \Sigma}{\delta G} = -I$. These are a cornerstone of Φ -derivable approaches [93], where $\frac{\delta \Phi}{\delta G} = \Sigma$, and $\frac{\delta^2 \Phi}{\delta G^2} = -I$. Since the functional derivative cannot be evaluated numerically, it mostly serves as a formal tool. However, by choosing a specific variation δG in the functional WI, one can derive more practical relations (as necessary but not sufficient conditions of the functional WIs). For instance, one can easily deduce Eq. (29) in the limit $\omega \rightarrow 0$ by varying G with respect to (w.r.t.) frequency (see Ref. [94] for a related treatment). Moreover, one can derive the standard fRG self-energy $\tilde{\Sigma}_{\text{std}}$ by varying G through the scale parameter [9].

Numerical results—Since the Pauli principle is preserved in the PA as well as (loop-converged) mfRG, one expects—on general grounds—these approximate schemes to violate the WIs to a certain extent. Arguably, the size of such violation should increase for increasing interaction strength, driven by the leading terms of the exact solution (where all fundamental relations are fulfilled), which are neglected in either approximate approach. Furthermore, it is known [10,18] that the 1ℓ truncation leads to violations of the WIs. Katanin [17] proposed schemes to mitigate this deficiency. In particular, the $1\ell_K$ flow is widely used and often argued to better fulfill WIs. However, no explicit numerical studies were presented thus far. Here, we intend to fill this gap and investigate *quantitatively* the fulfillment of WIs in fRG using our numerical results for the AIM. We focus on flowing (m)fRG results obtained with the Ω flow, in order to avoid the frequency extrapolation required for the U flow (see Appendix B 1).

We start with Fig. 12, where the top row shows $\mathcal{W}_L(\nu, \omega)$ (squares) and $\mathcal{W}_R(\nu, \omega)$ (hexagons) for $\omega = 2\pi T$ as a function of ν for $U = 1$, as obtained from the flow. We find that the 1ℓ result exhibits the *strongest deviation* in the WI for all ν ; $1\ell_K$ yields already a visible improvement at the lowest Matsubara frequency. However, the 2ℓ and mfRG/PA results show an overall much more accurate description of the WI for all frequencies. In particular, we note that while, at the lowest Matsubara frequency, the deviation in 2ℓ is smaller than in mfRG/PA, the trend is reversed for larger frequencies.

To better quantify the deviations between both sides of the WI, we focus on the quantity $\delta\mathcal{W}(\nu, \omega) = \mathcal{W}_L(\nu, \omega) - \mathcal{W}_R(\nu, \omega)$ at $\omega = 2\pi nT$ ($n \in \mathbb{N}$) for two different choices for ν : In the first case, we fix ν to $\nu_s = -[n/2]2\pi T + \pi T$, which gives the fermionic frequency closest to the symmetry axis $\nu = -\omega/2$, where the largest absolute deviations are found (e.g., $\nu_s = -\pi T$ for $\omega = 2\pi T$ in Fig. 12, see also Fig. 13 discussed below). In the second case, we sum $|\delta\mathcal{W}|$ for ν in a finite frequency box. Specifically, we sum over 11 frequencies to the left and 11 frequencies to the right of the symmetry axis, adding also the contribution right at $\nu = -\omega/2$ if n is odd. In this way, we incorporate the behavior at larger frequencies, while avoiding numerical inaccuracies from the finite-frequency box effect of the high-frequency parametrization in our implementation [6] (see Appendix B 1). When comparing results for different transfer frequency $\omega = 2\pi nT$, we divide by n to obtain more comparable results. The bottom row of Fig. 12 shows $\delta\mathcal{W}$ for the $n = 1$ data reported at the top. The plot confirms that, at weak coupling, already the first multiloop corrections strongly improve the fulfillment of the

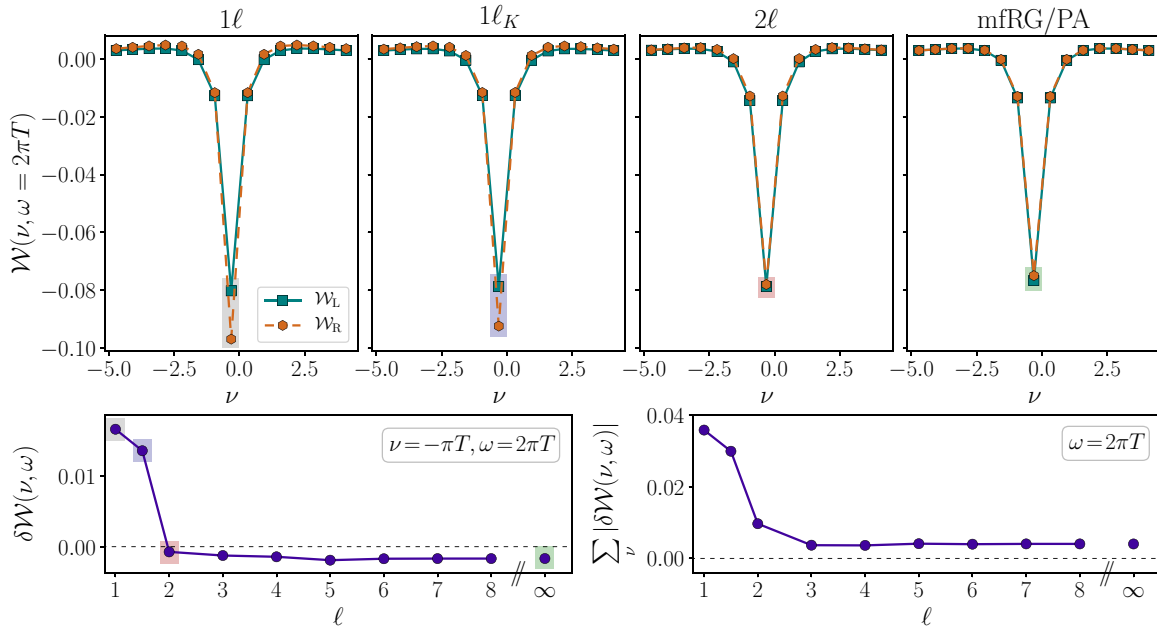


FIG. 12. Top: Comparison of the left side \mathcal{W}_L (teal, squares) and the right side \mathcal{W}_R (brown, hexagons) of the WI (29) for Ω -flow mfRG calculations, as a function of ν for $\omega = 2\pi T$ and $U = 1$ ($\beta = 10$ throughout). Bottom: Fulfillment of the WI estimated by $\delta\mathcal{W} = \mathcal{W}_L - \mathcal{W}_R$ as a function of loop order, for $\nu = -\pi T$ (left) and for ν summed over a finite box (right, see text). Colored areas in the upper and lower left panel mark equivalent data points.

WI. In particular, the minimal value for $\delta\mathcal{W}$ at $\nu = -\pi T$ (left panel) is found at $\ell = 2$ and for $|\delta\mathcal{W}|$ summed over ν (right panel) at $\ell = 3$. Hence, our $U = 1$ calculations show that the finite deviation from the exact fulfillment of the WI expected to occur in the loop-converged mfRG/PA results is notably smaller in comparison to 1ℓ or $1\ell_K$, and that it quantitatively represents a marginal effect in the weak-coupling regime. This trend is also confirmed regarding relative deviations $|\delta_r\mathcal{W}| = |\delta\mathcal{W}/\mathcal{W}_L|$, as we explicitly show in Fig. 19 in Appendix A.

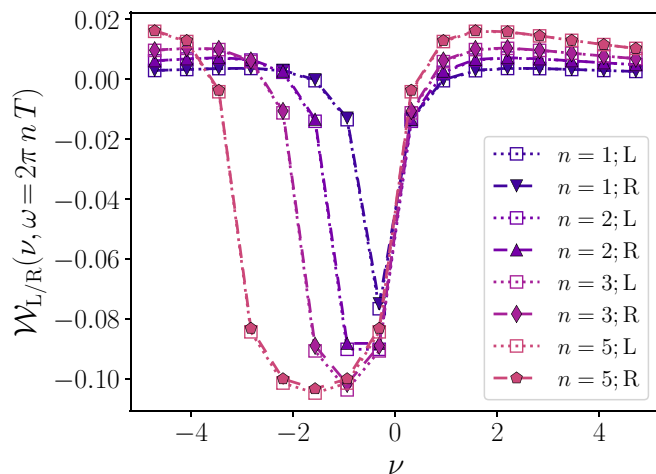


FIG. 13. \mathcal{W}_L (dotted lines, empty squares) and \mathcal{W}_R (dashed lines, filled symbols) of the loop-converged mfRG solution, as a function of ν , at $U = 1$ and for different values of $\omega = 2\pi n T$. The absolute discrepancy is largest for ν around $-\omega/2$.

Next, we extend the analysis to larger values of $\omega = 2\pi n T$ and show in Fig. 13 loop-converged mfRG results for $1 \leq n \leq 5$. The plot demonstrates that the mfRG data provide satisfactory agreement between \mathcal{W}_L (empty squares) and \mathcal{W}_R (filled symbols) for all values of ω and ν , and that the largest absolute deviation indeed occurs for ν around ν_s , i.e., the frequency closest to the symmetry axis $\nu = \omega/2$ (see above). Figure 14 presents $\delta\mathcal{W}$ as a function of ℓ for n up to 40. Again, the fulfillment of the WI is slightly improved when going from 1ℓ to $1\ell_K$ and strongly improved starting from 2ℓ , for all values of ω (confirmed also by Fig. 19 in Appendix A). However, the details in the change from $\ell = 2$ to ∞ depend on ω . In general, we observe that the WI is better fulfilled for larger values of ω . In fact, a perfect match is given for $\omega \rightarrow \infty$ and $\ell \rightarrow \infty$, since the WI reproduces the SDE for $\omega \rightarrow \infty$ (see Appendix C 2), which is exactly fulfilled in mfRG and the PA. This can be clearly seen in both insets of Fig. 14. The inset of the right panel uses a logarithmic scale, where one can also spot the onset of oscillations in the multiloop convergence, in spite of their small amplitude.

Finally, we analyze the effects of the interaction strength, by progressively increasing its value up to $U = 4$. In Fig. 15, we examine $\delta\mathcal{W}$ for $\omega = 2\pi n T$ at $n = 1$ and $n = 11$, comparing results of (m)FRG flows at low loop order with the PA. At large interaction, the pure 1ℓ flow is evidently unreliable, violating the WI with very large values of $\delta\mathcal{W}$. The situation visibly improves in $1\ell_K$, 2ℓ , and PA. In particular, for $U \leq 2$, $1\ell_K$ is farther off than 2ℓ and PA. Interestingly, however, the $1\ell_K$ deviations display a highly non-trivial behavior with increasing U —they are nonmonotonous in the top left panel and have a decreasing slope in the other panels—and thereby yield comparatively small values of $\delta\mathcal{W}$ at larger

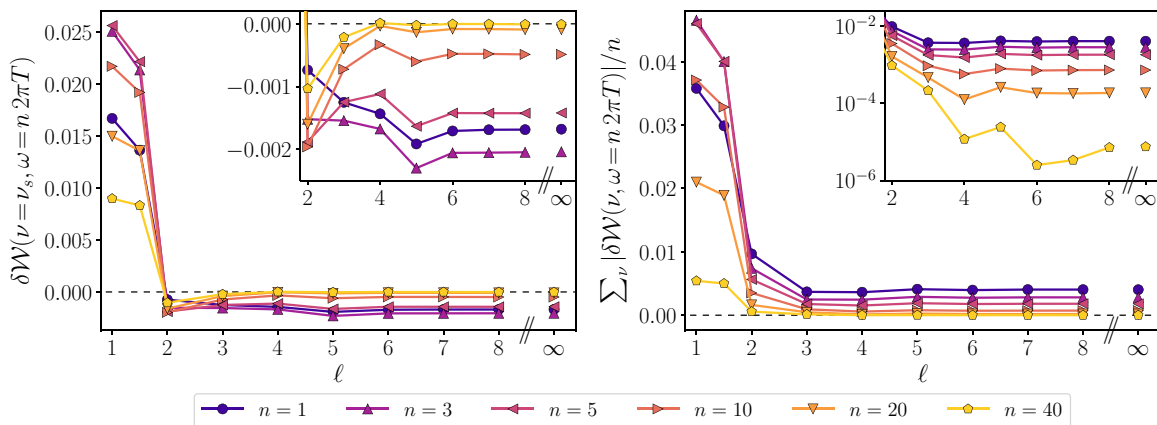


FIG. 14. $\delta\mathcal{W}$ in mfRG as a function of loop order at $U = 1$ for different values of $\omega = 2\pi nT$ and different choices for ν . Left: $\nu = \nu_s = -[n/2]2\pi T + \pi T$, which gives the fermionic frequency closest to the symmetry axis $\nu = -\omega/2$ where the largest absolute deviation is found. Right: ν is summed over a finite box (see text). Larger values of ω are shown in yellow, smaller ones in violet. The insets show a zoom starting at $\ell = 2$, using a linear (logarithmic) scale for the left (right) panel.

U . By contrast, for the PA results, $|\delta\mathcal{W}|$ starts rather small but increases monotonously with increasing U . Overall, for intermediate to large values of U , it seems that $1\ell_K$ provides the most accurate description of the WI at small frequencies ($n = 1$), while mfRG and the PA lead to a smaller violation of the WI for larger frequencies (here $n = 11$). Further details on the individual deviations of \mathcal{W}_L and \mathcal{W}_R are given in Appendix A.

As a last step, we compare the numerical deviations $\delta\mathcal{W}$ as a function of U focusing on small interaction values $U < 1$. Figure 16 shows $\delta\mathcal{W}$, similarly as in Fig. 15, but on a log-log scale. Using a $f(x) = \alpha x + d$ fit, we extract the exponents of the deviations of the WI, $\delta\mathcal{W} \sim U^\alpha$, for the (m)RG flow and PA scheme. Our analysis shows perfect agreement with the theoretical predictions of Ref. [17]: the 1ℓ scheme displays deviations that grow with the third power of U ($\alpha \approx 3$, solid lines), and the 2ℓ results are in agreement with a U^4 growth

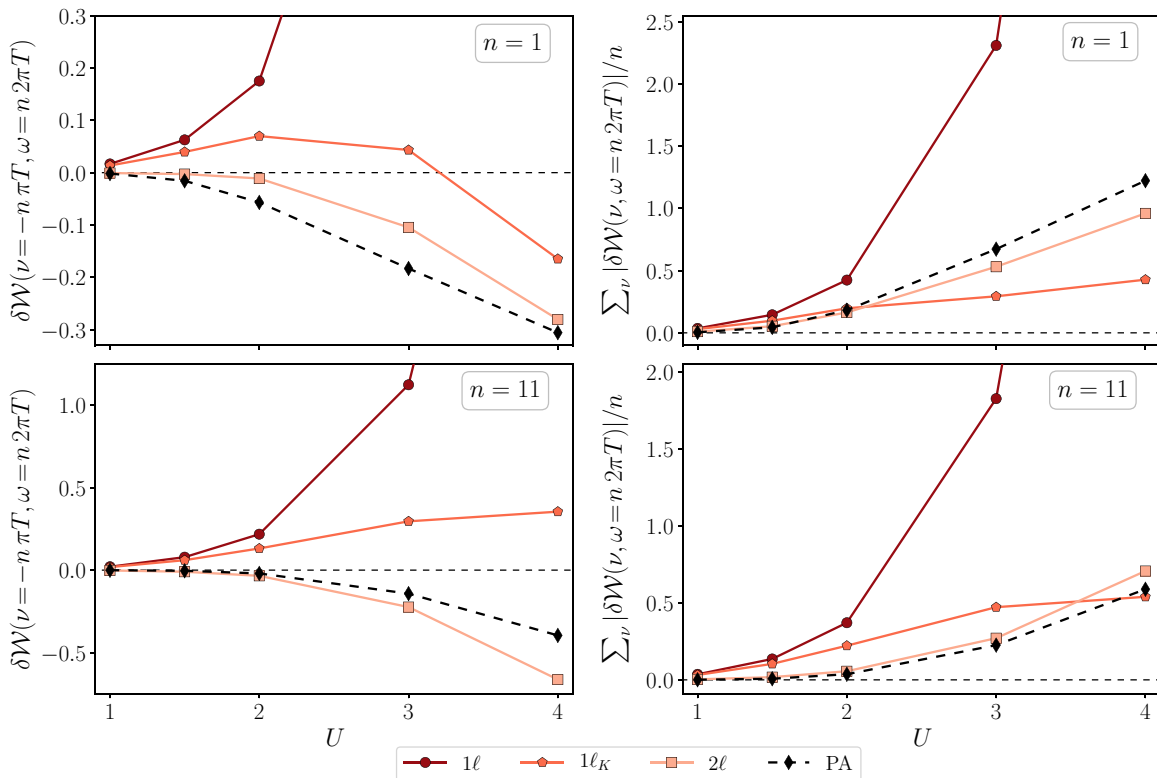


FIG. 15. $\delta\mathcal{W}$ for increasing U obtained with different methods. Solid lines in shades of red denote (m)fRG schemes (Ω flow) at low loop order; the PA solution is shown in dashed black. In the top (bottom) panels, $\omega = 2\pi nT$ is fixed at $n = 1$ ($n = 11$). In the left panels, we use $\nu = -\pi T$ ($\nu = -11\pi T$). In the right panels ν is summed over a finite box (see text).

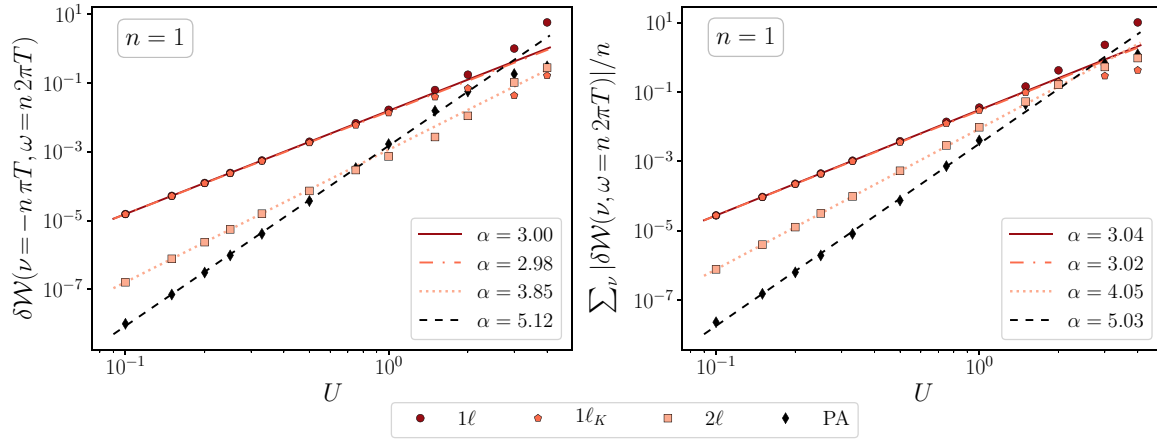


FIG. 16. Same as Fig. 15 for $n = 1$, but including data for very small interaction values $U < 1$, using a log-log scale. The straight lines correspond to $f(x) = \alpha x + d$ fits using the first data points between $U = 0.1$ and $U = 0.5$, yielding the exponents of the $\sim U^\alpha$ behavior.

($\alpha \approx 4$, dotted lines). The $1\ell_K$ results at small U also manifest $O(U^3)$ deviations. This is in agreement with the analytic arguments of Ref. [17] since, for the commonly used $1\ell_K$ scheme, only part of the 2ℓ corrections are included by substituting $S \rightarrow \tilde{G}$ (as described in Sec. II). Hence, some terms violating the WI at $O(U^3)$ remain, as seen in our numerical data in Fig. 16 ($\alpha \approx 3$, dashed-dotted lines). Note that the behavior at larger interaction values, as discussed above, is beyond the reach of the present analysis applicable at small values of U .

Further, concerning the loop-converged mFRG/PA results, we find deviations of the WI, which behave as $O(U^5)$ (dashed lines). In general, one expects the PA/mFRG schemes to deviate from the exact solution as $O(U^4)$. However, at half filling, the combination of the particle-hole symmetry and spin symmetry of our problem causes the contributions to the WI from the forth-order “envelope” diagrams to exactly cancel, as we show explicitly in Appendix C 3. For completeness, we also note that the same behavior as in Fig. 16 is found for other frequency choices as well (e.g., for $n = 11$ used in the lower panel of Fig. 15).

V. CONCLUSION AND OUTLOOK

We investigated several essential features of the recently introduced mFRG approach by performing a quantitative study of the particle-hole symmetric AIM for different coupling strengths. As the numerical implementation of the mFRG applied to the AIM does not require additional algorithmic approximations (such as the form factor expansion used for the Hubbard model [36,37]), we were able to demonstrate how the precise convergence of the mFRG series to the corresponding PA results is readily obtained in the entire weak- to intermediate-coupling regime. A thorough inspection further confirmed the pivotal features of a converged mFRG solution, i.e., its independence of the specific RG cutoff adopted as well as the equivalence between flowing and postprocessed results. Hence, in the parameter regimes where a fast loop convergence of the mFRG is found, the application of this method offers potential advantages w.r.t. to the full iterative solution

of the PA through the intrinsic flexibility of the underlying fRG framework.

By increasing the value of the electronic interaction, we studied the oscillatory behavior emerging in the loop dependence of the mFRG series, which eventually hinders the convergence to the PA solution in the strong-coupling regime. Interestingly, the parameter region where a multiloop convergence could not be achieved appears roughly to match the one in which previous quantum Monte Carlo studies [51,60] have shown an explicit breakdown of perturbative resummations to occur at the two-particle level. In this respect, the strong oscillatory behavior of the nonconverging mFRG series could be plausibly regarded as a further hallmark of the nonperturbative [51,75,76,78] parameter regime, where significant physical differences between the PA and the exact solution of the AIM are found [51].

The numerical data obtained in the region of proper convergence of the mFRG algorithm were then used for a quantitative investigation of the fulfillment of fundamental features of the many-electron problem, namely those linked to (i) the Pauli principle and (ii) the WIs. For (i) the Pauli principle, we observed a sizable violation of sum rules in the conventional 1ℓ fRG results, which gets systematically reduced by increasing the loop order. This is consistent with the fact that mFRG converges to the PA solution, and that the PA obeys the Pauli principle by construction, realized through the crossing symmetry and two-particle self-consistency. We also note that the indirect effects of the Pauli principle on the high-frequency asymptotic behavior of one-particle quantities are only recovered by including the multiloop additions to the self-energy flow, which start from the third loop onwards. For (ii) the WIs, these are generally neither fulfilled in fRG nor in the PA. For weak to intermediate coupling, our results demonstrated that adding higher-loop terms systematically reduces the overall violation of WIs. In particular, while a first improvement can be already observed by including the one-loop Katanin ($1\ell_K$) substitution, higher loop orders and the PA yield quantitatively much smaller deviations. By increasing the interaction, however, the situation becomes more complex. Going beyond

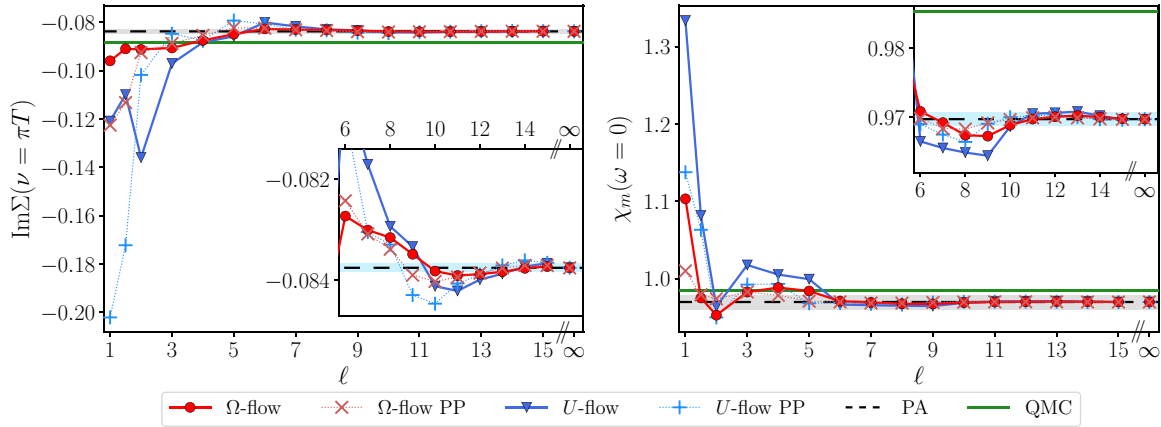


FIG. 17. $\text{Im}\Sigma(\nu = \pi T)$ and $\chi_m(\omega = 0)$ as in Fig. 4 but for $U = 1.5$. Insets show a zoom for $\ell \geq 6$. The gray (blue) area indicates 1% (0.1%) deviation from the PA.

the 1ℓ fRG level, whose description of the WIs is largely unreliable, we find that $1\ell_K$ mitigates most efficiently the WI violations at low frequencies, while higher-loop mFRG and the PA yield better results for large frequencies. This is consistent with our observation that the WI reproduces the SDE for $\omega \rightarrow \infty$. Additionally, we confirmed the predictions of Ref. [17] for the asymptotic weak-coupling behavior of the WI deviations as a function of U for the 1ℓ and 2ℓ scheme. Our numerical results for the mFRG/PA scheme revealed a $O(U^5)$ deviation, smaller than the expected $O(U^4)$, which we showed to be related to the particle-hole and spin symmetry used in our computations.

The insights gained in our study, which might be extended in the future to other regimes (e.g., out of half filling, and/or in the presence of a magnetic field) and more complex systems, are important for several reasons. On the one hand, they improve the understanding of the convergence of the mFRG procedure, whose relevance extends to more complex contexts than the basic AIM considered here. Such insights may be particularly important if the mFRG is used to include *nonlocal correlations* on top of the DMFT solution of strongly correlated lattice problems, thus extending the DMF²RG algorithms beyond the conventional (1ℓ) fRG used so far [52,53]. In that context, the mFRG might offer important advantages over corresponding parquet-based implementations. In contrast to the latter, the mFRG flow does *not* rely on the numerical manipulation of two-particle irreducible vertex functions, which display multiple divergences in the intermediate-to-strong coupling regime of different many-electron models [51,60,78–85]. This should allow the circumvention of several of the problems faced by parquet-based DMFT extensions [42] constructed upon such potentially diverging irreducible vertices, such as parquet D Γ A [4,95] or QUADRILEX [96].

On the other hand, the possible relation of the loop convergence properties in mFRG with the breakdown of the perturbation expansion might have interesting theoretical and algorithmic implications, calling for an extension of our study to more complex physical situations than those considered here. Together with our precise analysis of the fulfillment or violation of sum rules and WIs, this might shed new light on fundamental aspects of the many-electron theory and help

to further develop refined calculation strategies for the most challenging parameter regimes.

ACKNOWLEDGMENTS

The authors thank C. Eckhardt, S. Heinzelmann, A. Kauch, F. Krien, S. Jakobs, V. Meden, G. Rohringer, T. Schäfer, A. Tagliavini, and N. Wentzell for valuable discussions. We acknowledge financial support from the Deutsche Forschungsgemeinschaft (DFG) through Project No. AN 815/6-1 (S.A.) and through Germany’s Excellence Strategy EXC-2111 (Project No. 390814868) (J.v.D.), as well as from the Austrian Science Fund (FWF) through Project No. I 2794-N35 (P.C. and A.T.). Calculations were done in part on the Vienna Scientific Cluster (VSC). F.B.K. acknowledges support by the Alexander von Humboldt Foundation through the Feodor Lynen Fellowship.

APPENDIX

In the Appendix, we provide additional results, details on the numerical treatment as well as diagrammatic derivations, in order to specify our approach and further support the messages of the main part. The additional results are in Appendix A, mainly focused on the U flow and the fulfillment of the WI. Details on our numerical approach, especially the dependence of different quantities on the number of Matsubara frequencies included in the computations, are discussed in Appendix B. Finally, we give the diagrammatic derivations of several relations used in Sec. IV in Appendix C.

APPENDIX A: ADDITIONAL RESULTS

In Fig. 17, we report the results for $U = 1.5$ ($\beta = 10$, half filling), which were anticipated in Sec. III B. For this parameter set, too, the mFRG scheme converges perfectly in loop order. For $\ell \geq 15$, both regulators lead to identical results for all quantities, and the PP (dotted lines with “ \times ” or “ $+$ ” symbols) and flowing data coincide. As stated in the main text, no qualitative difference in the convergence behavior is observed, apart from the fact that, for $U = 1.5$, more loop orders are necessary to reach it.

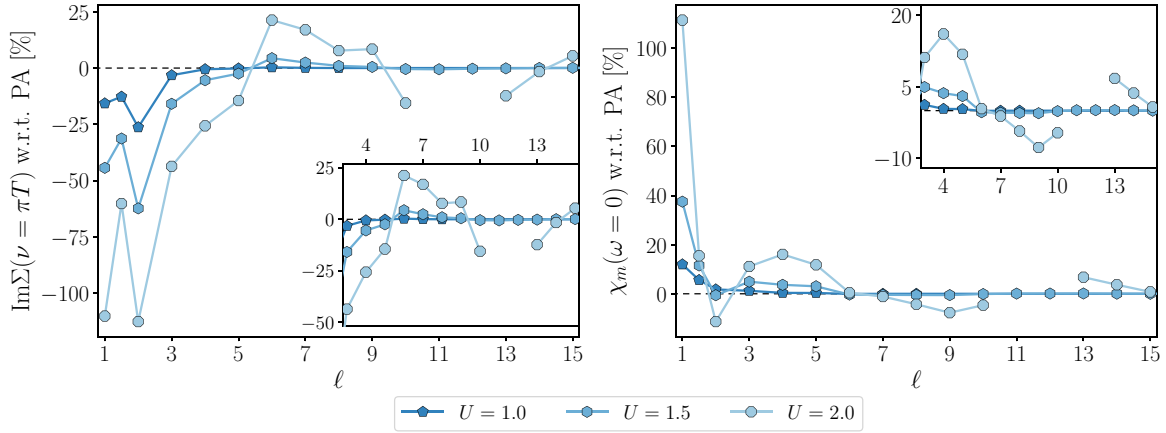


FIG. 18. Relative difference between U -flow mFRG calculations and the corresponding PA solutions for $\text{Im}\Sigma(\nu = \pi T)$ (left) and $\chi_m(\omega = 0)$ (right), as a function of loop order ℓ and different values of the interaction U , as in Fig. 6. Insets show a zoom for $\ell \geq 3$.

In Fig. 18, the relative comparison between U -flow results and the PA for $U = 1, 1.5, 2$ is shown in the same fashion as in Fig. 6 for the Ω flow. While there is no qualitative difference, quantitatively the U flow shows larger relative differences with respect to the PA. Note that we were unable to converge the U -flow calculation for $\ell = 11, 12$; see also Appendix B 2.

Finally, we add further analyses on the fulfillment of the WI, namely (i) on the relative deviations for the cases discussed in the main text, and (ii) more details on the deviations as a function of U in the different approaches. Concerning (i), Fig. 19 is a combined plot of Figs. 12 and 14 of the main text, but instead of $\delta\mathcal{W}$, we show $|\delta_r\mathcal{W}(\nu, \omega)| = |\mathcal{W}_L(\nu, \omega) - \mathcal{W}_R(\nu, \omega)/\mathcal{W}_L(\nu, \omega)|$. In the top row, $|\delta_r\mathcal{W}|$ is shown for $\omega = 2\pi T$, similarly as in the top row of Fig. 12. Note that the y axis is cut at $|\delta_r\mathcal{W}|=100\%$ in order to present the behavior of $|\delta_r\mathcal{W}(\nu, \omega=2\pi T)|$ for the various values of ν with sufficient resolution. The reason for the peak of $|\delta_r\mathcal{W}|$ at one specific Matsubara frequency is the sign change (and hence the closeness to zero) of $|\mathcal{W}_L|$. The bottom panels and the corresponding insets show the relative deviation $|\delta_r\mathcal{W}(\nu, \omega=n2\pi T)|$ for $\nu = \nu_s$ (left) as well as for an averaged sum over a finite frequency box (see main text for both). Due to the averaging effect of the factor $1/N_\nu$ in $\frac{1}{N_\nu} \sum_\nu |\delta_r\mathcal{W}(\nu, \omega=n2\pi T)|$, where N_ν is the number of elements summed over, the factor $1/n$ used in Fig. 14 is omitted. In general, Fig. 19 confirms the trend described in the main text. One notices how the increase of the loop order ℓ leads to a reduction of the relative deviations for all frequencies ω and ν . As pointed out in Sec. IV, the WI is exactly fulfilled for the mFRG/PA solution at $n \rightarrow \infty$, which is also confirmed in Fig. 19 (see insets). An important difference to Fig. 14 is that for the $1\ell, 1\ell_K$ and 2ℓ scheme, $\delta_r\mathcal{W}(\nu = \nu_s, \omega)$ is roughly constant, or even grows as n is increased. This reflects the fact that these approaches do not respect the SDE, and hence do not fulfill the WI exactly for $n \rightarrow \infty$. Regarding (ii), we use the numerically exact QMC solution (fulfilling the WI) as a reference and compare \mathcal{W}_L and \mathcal{W}_R obtained by fRG/PA for $\nu = \nu_s$ (see main text) individually with the QMC result. Figure 20 shows this analysis for different values of U , in a similar fashion as Fig. 15. The comparison of the left side, $\Delta\mathcal{W}_L = \mathcal{W}_L^\chi(\nu = \nu_s, \omega) - \mathcal{W}_L^{\text{QMC}}(\nu = \nu_s, \omega)$, where

χ represents the given approach, is shown as full symbols with solid lines; the one of the right side, $\Delta\mathcal{W}_R = \mathcal{W}_R^\chi(\nu = \nu_s, \omega) - \mathcal{W}_R^{\text{QMC}}(\nu = \nu_s, \omega)$, as empty symbols with dashed lines, where $\mathcal{W}_L^{\text{QMC}}(\nu, \omega) = \mathcal{W}_R^{\text{QMC}}(\nu, \omega)$. Let us point out that two distinct effects need to be distinguished in Fig. 20: On the one hand, there are the deviations of the fRG/PA results from the numerically exact QMC results, on the other hand, the fact that the fRG/PA results do not fulfill the WIs, and are hence not conserving. As discussed in the main part in Fig. 7, the deviations between PA/fRG calculations and the QMC results grow with U , which can also be seen in Fig. 20. The solution of a conserving approximation would show this deviation, but would not show a difference between the left and right side, i.e., the full and the dashed lines would coincide. Hence, it is not the value on the y axis itself, but the difference in the deviation of $\Delta\mathcal{W}_L$ and $\Delta\mathcal{W}_R$, which turns out to be instructive. As can be seen in Fig. 20, for most cases, it is the right side of the WI that deviates more from the QMC solution, the Ω -flow $1\ell_K$ -results for $n = 11$ represent the extreme case. While in the PA, the 1ℓ and 2ℓ results show a steadily growing difference between the solid and the dashed line, the situation is less monotonous for the $1\ell_K$ approach. From its data for $n = 1$ (top), one clearly notices the change in behavior as $\Delta\mathcal{W}_R$ changes sign, leading to the sign change of $\delta\mathcal{W}_L^{1\ell_K}(\nu = -\pi T, \omega = 2\pi T)$ seen in Fig. 15.

APPENDIX B: DETAILS ON THE NUMERICAL APPROACH

1. fRG and mFRG calculations

Our fRG, mFRG, and PA computations for the AIM are based on the implementation used in Refs. [6,36]. As stated in the main text, we employ the following parametrization of the reducible vertex functions [6] $\gamma_r = K_{1r} + K_{2r} + K_{2r} + K_{3r}$. The high-frequency asymptotics are included in the K_{1r} and $K_{2\omega_r}$ functions with one and two frequency arguments, respectively. The remaining full frequency dependence, which has a relevant contribution at low Matsubara frequencies, is contained in K_{3r} . These contributions increase with increasing interaction values, and it is hence necessary to extend the

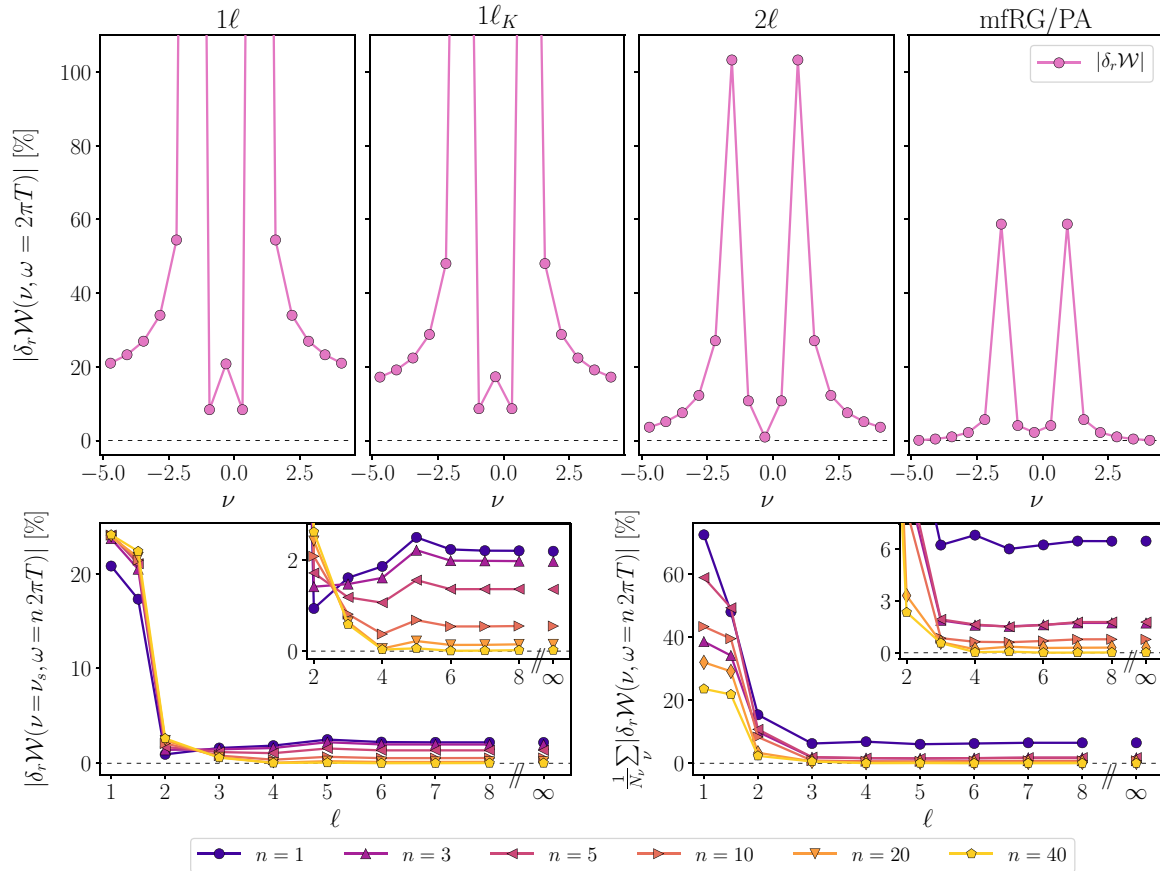


FIG. 19. Top: Relative deviation of the WI (29) $|\delta_r \mathcal{W}(\nu, \omega)| = |\delta \mathcal{W}(\nu, \omega) / \mathcal{W}_L(\nu, \omega)|$ for Ω -flow mFRG calculations at $\omega = 2\pi T$, $U = 1$, similarly as the top row panels of Fig. 12, as a function of ν . The y axis is cut at 100% to provide enough resolution for $|\delta_r \mathcal{W}(\nu, \omega = 2\pi T)|$ at the various values of ν . Bottom: As Fig. 14 but showing $|\delta_r \mathcal{W}|$ instead. In the right panel, the normalizing factor $1/n$ of the main text is replaced by $1/N_\nu$, where N_ν is the number of frequencies summed over (see text). All quantities are given in percent (%).

frequency box, i.e., the number of frequencies where the full frequency dependence of K_{3r} is taken into account. In Table I, we provide the number of positive fermionic frequencies of K_{3r} , N_{f_+} , for different approaches and values of U . The parameter N_{f_+} also dictates all other frequency ranges in the same way as detailed in Ref. [6]. Outside the finite frequency box, the K_{3r} functions are set to zero, which is the core of the high-frequency asymptotics approximation. While this affects all quantities calculated with the different approaches, the

difference in the results observed by comparing computations with different box sizes is negligible for the Ω flow and PA. By contrast, for the U flow, an extrapolation in N_{f_+} is necessary, as detailed in the following subsection.

a. Frequency extrapolation for the U -flow

In order to achieve agreement between the ∞ -loop mFRG solution using the U flow and the corresponding PA result to the precision chosen in the main part of the paper (0.1% in the insets), it is necessary to perform a frequency extrapolation. To this end, several calculations for the same parameter set are performed with different sizes of N_{f_+} (see Table I). In Fig. 21, we showcase this for $U = 1$ and $\beta = 10$, i.e., the case discussed in Sec. III A. The open blue symbols represent the results for $\text{Im}\Sigma(\nu = \pi T)$ as obtained by different ∞ -loop U -flow calculations, plotted as a function of $1/N_{f_+}$. For comparison, the results of corresponding PA calculations with different box sizes are shown as open black symbols, which hardly display any dependence on N_{f_+} at this scale. Using a $f(x) = A + B/x$ fit (blue line), we obtain the extrapolated value (filled-blue triangle), which lies on-top of the PA result for $N_{f_+} = 32$ (dashed-black line). For comparison, we also plot the result of an ∞ -loop Ω -flow calculation (open red circle) using $N_{f_+} = 32$, which highlights

TABLE I. Number of positive fermionic Matsubara frequencies used in the calculations of the full frequency dependence (K_{3r}). For the PA calculations, we used the same number as for the Ω flow.

U	Flow	N_{f_+}
1.0	Ω	32
	U	32, 40, 64, 82
1.5	Ω	36
	U	32, 36, 40, 44
2.0	Ω	40
	U	36, 40, 44
3.0	Ω	52
	U	52

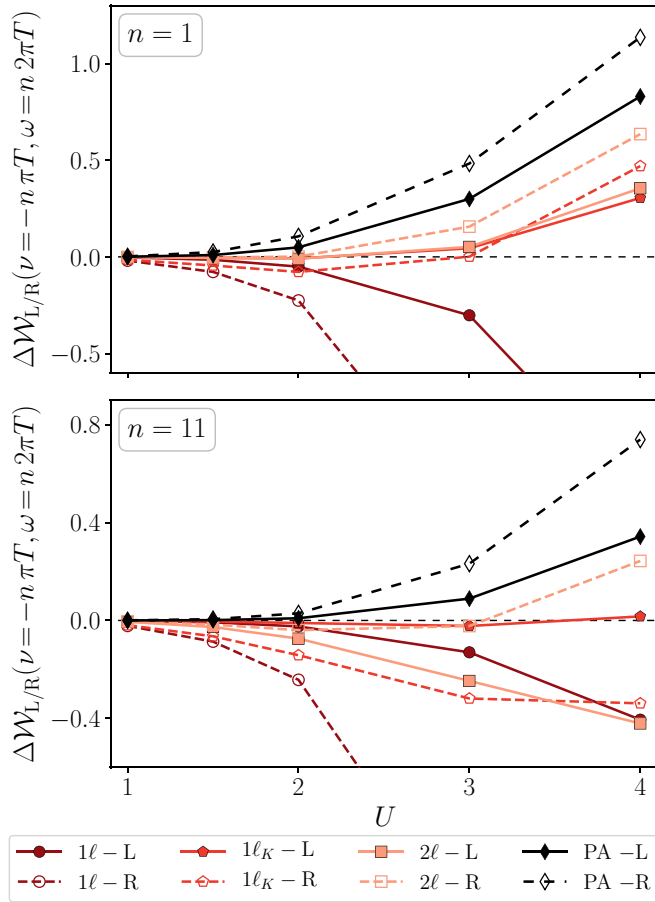


FIG. 20. $\Delta W_{L/R}$ as a function of U for different approaches where $\omega = 2\pi nT$ is fixed at $n = 1$ ($n = 11$) in the top (bottom) panel. The solid (dashed) lines represent the left (right) side of the WI in comparison with the QMC result, see text.

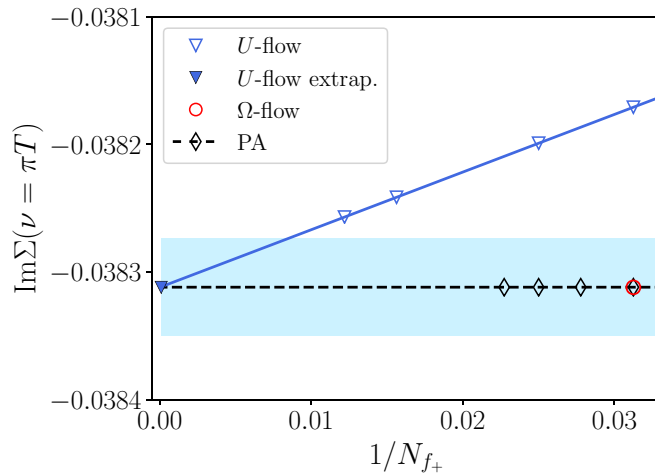


FIG. 21. $\text{Im}\Sigma(\nu = \pi T)$ as obtained by ∞ -loop U -flow calculations using different sizes of N_{f_+} , see Table I (open-blue triangles). The extrapolated value (filled blue triangle) is obtained using a $f(x) = A + B/x$ fit (blue line), which matches perfectly the PA solution for $N_{f_+} = 32$ (black-dashed line). The results of PA computations using different box sizes ($N_{f_+} = 32, 36, 40, 44$) are shown as open-black diamonds. The blue-shaded area represents 0.1% deviation from the PA solution for $N_{f_+} = 32$. For a comparison a ∞ -loop Ω -flow result using $N_{f_+} = 32$ (red-open circle) is also shown.

TABLE II. Maximum number of loops (ℓ_{\max}) and iterations of Σ ($N_{\Sigma\text{-iter}}$) needed for the ∞ -loop mFRG solution. In addition, for all interaction values, we list the number of Runge-Kutta integration steps in Λ during the fRG flows (N_{step}), and for the PA, the number of iterations need to reach convergence ($N_{\text{PA-iter}}$). Where no ∞ -loop mFRG solution was obtained, we list $N_{\Sigma\text{-iter}}$ and N_{step} of the calculations with $\ell = 15$. We reduced $N_{\Sigma\text{-iter}}$ for $U = 3$ for the Ω ($\ell = 15$) calculation, see text.

U	Flow	ℓ_{\max}	$N_{\Sigma\text{-iter}}$	N_{step}	$N_{\text{PA-iter}}$
1.0	Ω	15	3	54	
	U	23	4	9	
	PA				27
1.5	Ω	44	5	61	
	U	61	5	14	
	PA				43
2.0	Ω ($\ell = 15$)		8	69	
	U ($\ell = 15$)		9	23	
3.0	PA				56
	Ω ($\ell = 15$)		3*	98	
	PA				129

that, for the Ω flow, no frequency extrapolation is necessary to reach agreement with PA at this precision, as stated above.

All U -flow results for all loop orders shown in the main text and the Appendix are obtained in this way. For all quantities, a $f(x) = A + B/x$ fit proved to work best, except for the high-frequency value of Σ discussed in Sec. IV A (no U -flow results shown), where a $A + B/x + C/x^2$ fit turned out to be the best choice.

2. mFRG calculations

In this part of the Appendix, we provide further details on our multiloop calculations. In particular, we specify how the ∞ -loop mFRG solution is obtained and concisely discuss the iteration of Σ .

a. ∞ -loop mFRG solution

At each step of the fRG flow, the changes in all quantities for all Matsubara frequencies when going from ℓ to $\ell + 1$ are measured. As soon as the relative (absolute) changes are lower than a given ϵ , in our case 10^{-5} (10^{-7}), the calculation of higher loop orders is stopped. This speeds up the computation especially at the beginning of the flow, where usually a low loop order is sufficient; for more details on this, see Ref. [97]. While for obtaining the solution of loop order ℓ , the multiloop calculation is stopped at this specific ℓ , it is continued until the changes are smaller than ϵ to calculate the ∞ -loop order solution. In Table II, we provide the actual number of loops needed (ℓ_{\max}) to obtain the ∞ -loop order solution for the different flows and parameter sets.

b. Iteration of Σ

Part of the mFRG scheme is also the iteration of Σ at each step of the flow [9, 15, 16]. The effect of these self-energy iterations was analyzed in great detail in Ref. [37]. Throughout our calculations, their impact proved to be small, e.g., comparing

$\chi_m(\omega = 0)$ with and without the iteration of Σ for the Ω flow at $U = 1$ leads to a difference of $\mathcal{O}(10^{-4})$. In Table II, we provide the necessary number of iterations for the ∞ -loop mfRG solution ($N_{\Sigma\text{-iter}}$) to arrive at differences smaller than ϵ (given above, see Appendix B 2 a) when comparing iteration i with $i + 1$. For all other loop orders, the same condition was used. As it turns out, the number of necessary iterations proved to be very similar, except for the $\ell = 11, 12$ U -flow calculations for $U = 2$. There, the number of required Σ iterations increased considerably, preventing our numerical calculation from converging in a reasonable amount of time. Lowering the maximum number of Σ iterations did not allow for obtaining a converged result, as the adaptive solver used for our computations did no longer converge in this case.

For completeness, Table II also lists the number of Runge-Kutta integration steps in Λ during the fRG flow for both regulators (N_{step}), as well as the number of PA iterations ($N_{\text{PA-iter}}$). Note that, since the calculations for $U = 3$ were numerically very costly, as they required a large frequency box for K_{3r} , we restricted the number of iterations for the Ω -flow computations shown in the main part to 3.

3. QMC calculations

As stated in the main part, we employed the w2DYNAMICS [69] package (version 1.0.0) as a continuous-time QMC [39] solver. We used the default sampling method for all calculations shown apart from the data for Fig. 11. There, we performed Worm sampling [98,99] computations with symmetric improved estimators [100] instead, which reduces the high-frequency noise. While we used about 2000 CPU hours for the former computations, the Worm sampling calculations were done using up to 25 000 CPU hours.

APPENDIX C: DIAGRAMMATIC DERIVATIONS

1. Relations between the self-energy asymptote and the susceptibility sum rule

In this section, we will derive relations between the high-frequency asymptote of Σ and the sum rule of $\chi^{\sigma\sigma}$. First, we will show that the two are directly related through the SDE in parquet-type approaches. Then, we move on to fRG flows. We will show that the standard self-energy flow also relates the Σ asymptote to the susceptibility sum rule, with $\chi^{\sigma\sigma}$ given by its one-loop flow. Since the latter does not fulfill the sum rule, the former violates the exact asymptote. Both the sum rule and the asymptote are fulfilled in multiloop fRG. We will show which terms of the multiloop corrections to Σ complete the relation, so that the Σ asymptote is determined by $\chi^{\sigma\sigma}$ obtained in a multiloop flow. The entire derivation will proceed diagrammatically.

a. Connection through the SDE

In Fig. 22(a) we recall Eq. (18), which expresses $\chi^{\sigma\sigma}$ through a GG bubble and corrections in terms of the full four-point vertex F . The vertex F is contracted by pairs of propagators on both sides. Therefore, one can also express $\chi^{\sigma\sigma}$ through a (full) three-point vertex λ on either the left or the right side, as illustrated in Fig. 22(b). The vertex λ is

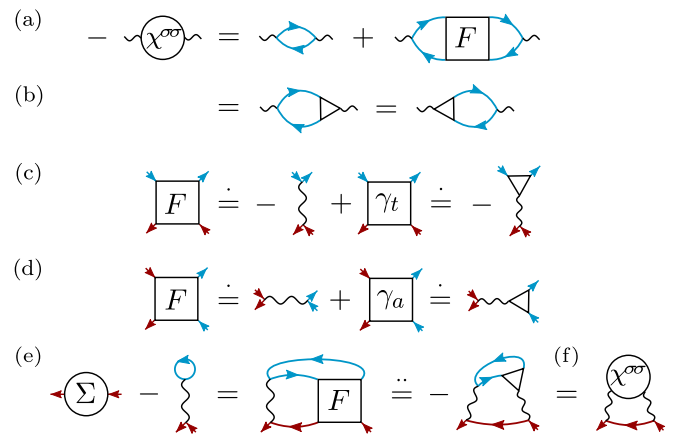


FIG. 22. [(a),(b)] The susceptibility $\chi^{\sigma\sigma}$ can be expressed through the four-point vertex F or the three-point vertex λ . [(c),(d)] In the limit $\nu \rightarrow \infty$, the vertex, carrying ν on the external legs marked in red, collapses to a subset of diagrams up to corrections $\mathcal{O}(1/\nu)$ (signified by “ \doteq ”). These can also be expressed through λ . [(e),(f)] In this limit, we can deduce the self-energy Σ_ν up to corrections $\mathcal{O}(1/\nu^2)$ (signified by “ \doteq ”) from the SDE and express the result through λ or $\chi^{\sigma\sigma}$.

particularly useful when considering F in the limit of large fermionic frequencies.

Indeed, to find the self-energy asymptote, we will consider a large fermionic frequency ν . In Figs. 22(c) and 22(d), we show which diagrams of the vertex F , carrying ν on the external legs marked in red, remain nonzero in the limit $\nu \rightarrow \infty$, i.e., which diagrams are independent of ν . We use the symbol “ \doteq ” for that purpose, signifying equality up to $\mathcal{O}(1/\nu)$. To have nonzero contributions when $\nu \rightarrow \infty$, the red (amputated) external legs must directly meet at a bare interaction vertex. This is clearly fulfilled for $F = F_0$, but there can also be arbitrary vertex corrections after the two red legs have met. If ν is on the lower two legs [Fig. 22(c)], such corrections are a subset of the vertex γ_t , reducible in *transverse* (vertical) particle-hole lines. If it is on the left two legs [Fig. 22(d)], the corrections belong to γ_a , reducible in *antiparallel* (horizontal) lines. The bare vertex and the corrections are summarized by the three-point vertex λ . To see this, one may insert the BSEs for $\gamma_{t/a}$, connecting the irreducible vertices $I_{t/a}$ to the full vertex F . Since $I_{t/a}$ are irreducible in their respective channels, they collapse to F_0 in the limit $\nu \rightarrow \infty$, and one obtains λ similarly as in going from Fig. 22(a) to Fig. 22(b).

Now, by means of the SDE (26), the self-energy (minus its static Hartree part) is determined by the vertex F connected to three propagators, as we recall in Fig. 22(e). To find Σ to first order in $1/\nu$, we need F to zeroth order. We choose to transport ν through the propagator at the bottom. Then, we can directly use the relation in Fig. 22(c) to replace F by λ up to corrections $\mathcal{O}(1/\nu^2)$ (signified by the symbol “ \doteq ”). Using Fig. 22(a), we obtain $\chi^{\sigma\sigma}$ through λ . The last step is similar to Eq. (27): Take the red propagator as $G_{\nu+\omega}^{\bar{\sigma}}$. For $\nu \gg \omega$, we can replace $G_{\nu+\omega}^{\bar{\sigma}}$ by $1/(i\nu)$ up to corrections $\mathcal{O}(1/\nu^2)$. This leaves $\chi_{\omega}^{\sigma\sigma}$ summed over all ω , and, with a prefactor U^2 from the two interaction lines, we obtain Eq. (25) for $\Sigma^{\bar{\sigma}}$.

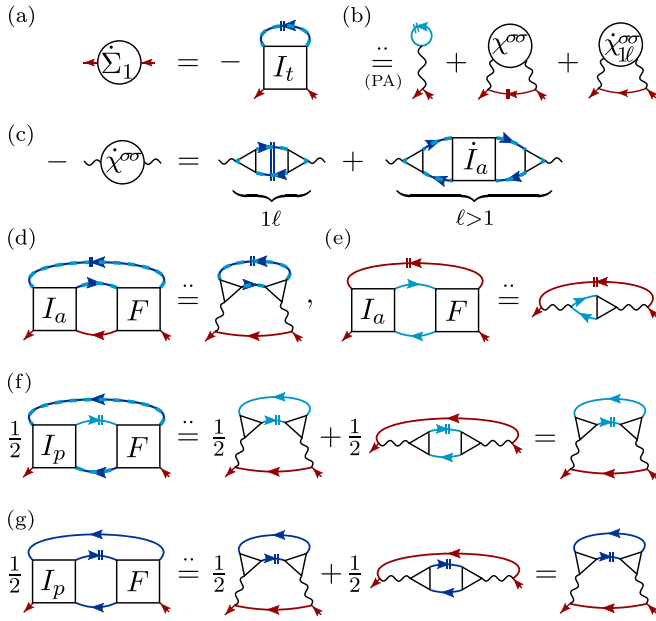


FIG. 23. (a) The standard self-energy flow $\dot{\Sigma}_{\text{std}} \equiv \dot{\Sigma}_1$ in skeleton form [9]. (b) In the PA, it yields asymptotic contributions of the same structure as Fig. 22(f), where $\dot{\chi}^{\sigma\sigma}$ is approximated by its one-loop flow. (c) One-loop ($\ell=1$) and multiloop terms ($\ell>1$) for $\dot{\chi}^{\sigma\sigma}$ [9]. To derive the relation in (b), we insert the BSEs for γ_a, γ_p as part of I_i ; [(d),(e)] concerns γ_a , [(f),(g)] concerns γ_p .

b. Standard self-energy flow

Next, we turn to fRG flows. The standard self-energy flow is given by $\dot{\Sigma}_{\text{std}} = -F^{\sigma\sigma'} \cdot S^{\sigma'}$, where “ \cdot ” denotes the contraction of the top two vertex legs by the following propagator, S is the single-scale propagator, and a sum over σ' is understood. For formal derivations, it is helpful to analyze $\dot{\Sigma}_{\text{std}}$ by means of its equivalent skeleton version [9], $\dot{\Sigma}_1^\sigma = -I_t^{\sigma\sigma'} \cdot \dot{G}^{\sigma'}$, illustrated in Fig. 23(a). As before, a line with a doubled orthogonal slash denotes \dot{G} , and dashed dark and light colors indicate a summation over spin.

As mentioned previously, $\dot{\Sigma}_1$ is exact only for an exact vertex, which is not available in practice. Instead, we will consider the much more relevant case of a vertex obtained in the PA or, equivalently, a multiloop flow. In this case, $\dot{\Sigma}_1$ is approximate. We will show that it generates a high-frequency asymptote of similar type as the exact relation Fig. 22(f), but with $\chi^{\sigma\sigma}$ obtained by its (approximate) one-loop flow. The connection from the general, Λ -independent statement Fig. 22(f) to an fRG flow is made by taking the scale derivative ∂_Λ on the entire equation. In this way, ∂_Λ is subsequently applied to the trivial Hartree part, to the red propagator alongside $\chi^{\sigma\sigma}$, and finally to $\chi^{\sigma\sigma}$ itself. Indeed, we will precisely find such a structure, where the derivative $\partial_\Lambda \chi^{\sigma\sigma}$ is approximated by $\dot{\chi}_{1\ell}^{\sigma\sigma}$, see Fig. 23(b). The one-loop flow $\dot{\chi}_{1\ell}^{\sigma\sigma}$ is given by the first summand of Fig. 23(c). (The long double slash denotes a differentiated two-particle propagator, $\dot{\Pi} = \dot{G}G + G\dot{G}$). The multiloop corrections to $\dot{\chi}^{\sigma\sigma}$, which are compactly encoded in the second summand of Fig. 23(c) and will be considered more closely in the next part, restore equivalence to the general susceptibility–vertex relation shown in Fig. 22(a).

To derive Fig. 23(b), we start from $I_t = F_0 + \gamma_a + \gamma_p$ in the PA. The bare vertex F_0 immediately gives the differenti-

ated Hartree part as the first summand of Fig. 23(b). From Fig. 23(d) onward, we analyze the effect of $\gamma_{a/p}$ using their BSEs. The analysis is slightly more complicated than in Fig. 22(e): There, we had just a single vertical interaction line; now, we have two spin-dependent vertices, where same-spin propagators can meet both vertically and horizontally.

In Figs. 23(d) and 23(e), we insert the BSE of $\gamma_a^{\sigma\sigma'}$, with a summation on the spin carried by $\dot{G}^{\sigma'}$. This gives three terms: (i) $\gamma_a^{\sigma\bar{\sigma}}$, where the antiparallel two-particle propagator Π_a necessarily has two opposite spins; $\gamma_a^{\sigma\sigma}$, where Π_a has (ii) both spins equal to σ and (iii) both spins equal to $\bar{\sigma}$. Cases (i) and (ii) are contained in Fig. 23(d), with a spin sum encoded in the dashed colors. Regarding $\sim v^{-1}$ contributions, Fig. 23(d) contains all diagrams where the lower two legs of I_a and F directly meet at vertical interaction lines and the large frequency is transported through the bottom propagator. Since both I_a and F contain $F_0 + \gamma_t$, their $\sim v^0$ contributions are expressed through λ according to Fig. 22(c). Proceeding with case (iii), Fig. 23(e) contains all diagrams where the left (right) legs of I_a (F) directly meet at horizontal interaction lines and the large frequency is transported through the top propagator. While F contains both F_0 and γ_a , I_a contains only F_0 . Hence, their $\sim v^0$ contributions are expressed through λ and a bare interaction line, respectively, according to Fig. 22(d).

We continue with γ_p and insert in Fig. 23(f) the BSE of $\gamma_p^{\sigma\bar{\sigma}}$ (\dot{G} is in light color), where the parallel two-particle propagator Π_p is summed over both spins (and thus the typical prefactor $1/2$ is kept). Since both I_p and F are crossing symmetric, contributions stemming from vertical and horizontal interaction lines enter equivalently. Indeed, in the first (second) summand of Fig. 23(f), the red propagator passes by vertical (horizontal) interaction lines. Since both I_p and F contain $F_0 + \gamma_a + \gamma_t$, we replace their $\sim v^0$ contributions by λ using Figs. 22(c) and 22(d), and we end up with two equivalent terms. In Fig. 23(g), we insert the BSE of $\gamma_p^{\sigma\sigma}$, where Π_p must also carry spins σ (the prefactor $1/2$ remains). Again, the red propagator can pass by vertical and horizontal interaction lines, and we get two equivalent terms expressed through λ .

Finally, we see that Fig. 23(e) gives the second summand of Fig. 23(b) [by means of Fig. 22(b)], and the sum of Figs. 23(d), 23(f), and 23(g) reproduces the first summand of Fig. 23(c). This yields the last part of Fig. 23(b), thus concluding the derivation.

c. Multiloop corrections to the self-energy flow

The multiloop corrections to the self-energy flow provide equivalence to the SDE while working in the PA [9]. Thereby, the multiloop self-energy flow is guaranteed to generate the correct high-frequency asymptote. Its $\sim v^{-1}$ contribution must be equal to the scale derivative of Fig. 22(f), shown in Fig. 24(a). The multiloop self-energy flow can be written [9] as $\dot{\Sigma} = \dot{\Sigma}_1 + \dot{\Sigma}_2$, with $\dot{\Sigma}_1^\sigma = -I_t^{\sigma\sigma'} \cdot \dot{G}^{\sigma'}$ from before and $\dot{\Sigma}_2^\sigma = -\dot{\gamma}_{t,C}^{\sigma\sigma'} \cdot G^{\sigma'}$. Hence, Figs. 24(a) and 23(b) imply that Fig. 24(b) must hold.

It is interesting to analyze how Fig. 24(b) comes about. Through the spin sum and the composite nature of $\dot{\gamma}_{t,C}$, $\dot{\Sigma}_2$ has four contributions, stemming from $\dot{\gamma}_{a,C}^{\sigma\sigma}$, $\dot{\gamma}_{p,C}^{\sigma\sigma}$, $\dot{\gamma}_{a,C}^{\sigma\bar{\sigma}}$, and $\dot{\gamma}_{p,C}^{\sigma\bar{\sigma}}$. We will show that the first term already gives the desired

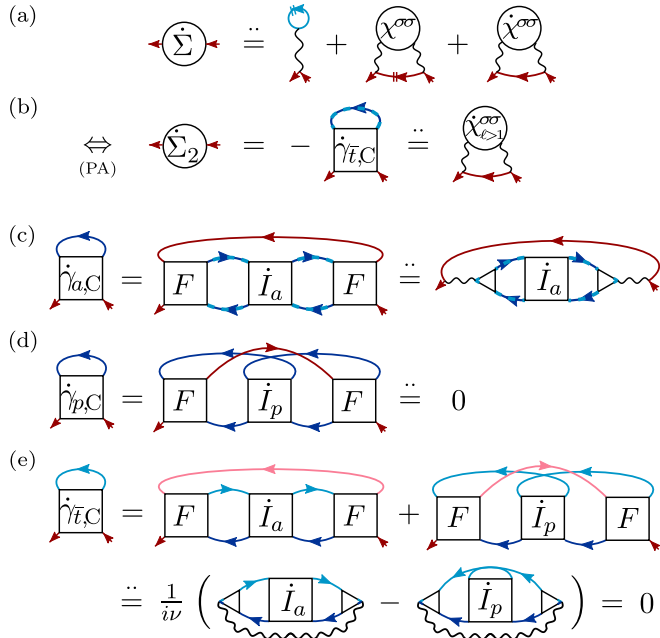


FIG. 24. (a) The multiloop self-energy flow is equivalent to the SDE and thus generates a high-frequency asymptote in direct correspondence to Fig. 22(f). (b) Using $\hat{\Sigma} = \hat{\Sigma}_1 + \hat{\Sigma}_2$ and the result of Fig. 23(b), the asymptote of $\hat{\Sigma}_2$ must be related to the multiloop corrections of $\hat{\chi}^{\sigma\sigma}$. To show this, we split the contraction of $\hat{\gamma}_{r,C}$ into four summands: (c) $\gamma_{a,C}^{\sigma\sigma} \cdot G^\sigma$ already yields the desired expression; (d) $\gamma_{p,C}^{\sigma\sigma} \cdot G^\sigma$ vanishes up to corrections $O(1/v^2)$; (e) $(\gamma_{a,C}^{\sigma\sigma} + \gamma_{p,C}^{\sigma\sigma}) \cdot G^\sigma$ cancel to that order, as can be seen after factoring out $G^\sigma \sim 1/(i\nu)$ for the first and $G^\sigma \sim 1/(-i\nu)$ for the second summand.

result in Fig. 24(b). Up to corrections $O(1/v^2)$, the second term vanishes while the last two terms cancel.

Inserting $\hat{\gamma}_{a,C}^{\sigma\sigma}$, the only way to get $\sim v^{-1}$ contributions is to transport the large frequency through the loop propagator at the top, marked red in Fig. 24(c) (note that both two-particle propagators Π_a are summed over spin). Further, all red lines must directly meet at (horizontal) interaction lines. Hence, the four-point vertices F at the left and right can be replaced by three-point vertices λ . The combination of $\lambda, \dot{I}_a, \lambda$ comprises the multiloop corrections to the flow of $\chi^{\sigma\sigma}$, see Fig. 23(c), thus yielding Fig. 24(b).

For the remaining terms, one immediately sees in Fig. 24(d) that $\hat{\gamma}_{p,C}^{\sigma\sigma}$ has no $\sim v^{-1}$ contribution: The external legs and the loop propagator would need to directly meet as two out-going (in-going) lines at a bare interaction line of the left (right) vertex. However, they all have the same spin, and the bare interaction requires in- and out-going lines to have opposite spin. Next, the opposite-spin contribution $\hat{\gamma}_{a,C}^{\sigma\bar{\sigma}} + \hat{\gamma}_{p,C}^{\sigma\bar{\sigma}}$ is shown in Fig. 24(e). By choosing fixed spin labels for the two Π_p entering $\hat{\gamma}_{p,C}$, we eliminate the typical prefactor $(1/2)^2$. The upper loop propagator carrying the ν dependence goes in opposite directions for the first compared to second summand. Hence, after factoring out the dominant $1/(i\nu)$, we get opposite signs for the $\sim v^{-1}$ contributions between the a and p channel. The remaining part for both is summed over all internal frequencies, including ω , as indicated by the closed wiggly line. Their sum cancels, as can be checked explicitly

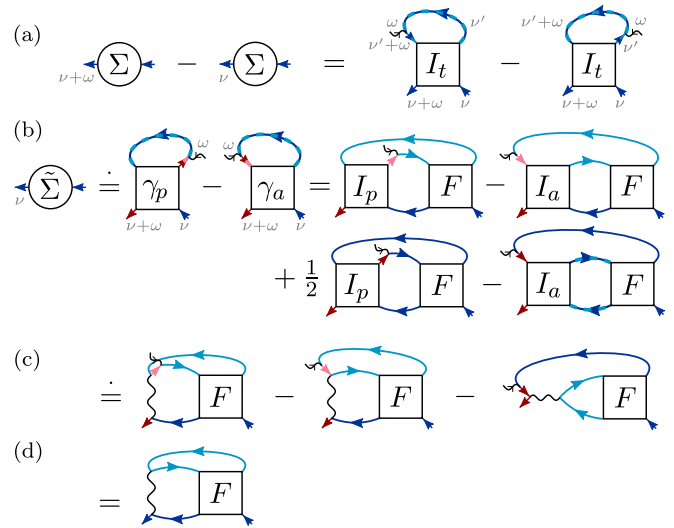


FIG. 25. (a) Illustration of the WI (C1), in a slightly different but equivalent form to Fig. 8(c). Note that short lines denote amputated legs, which are not part of the equation. (b) Derivation of the SDE from the WI by taking the limit $\omega \rightarrow \infty$, see text. Lines in red colors carry the large frequency ω .

at low orders. Note that, for this to work, one needs the same number of diagrams in $\gamma_a^{\sigma\bar{\sigma}}$ and $\gamma_p^{\sigma\bar{\sigma}}$ at each interaction order, as is indeed the case [101].

2. Deriving the SDE from the WI

The WI (29) relates a difference of self-energies, $\Sigma_{\nu+\omega}^\sigma - \Sigma_\nu^\sigma$, to a vertex contracted by a combination of propagators. For infinitely large ω , while ν remains finite, the first self-energy simplifies to its static value, $\Sigma_{\nu+\omega}^\sigma \rightarrow Un_{\bar{\sigma}}$, and we thus obtain a relation for Σ_ν^σ alone. This relation is precisely the SDE (26), as we show now.

We start by restating Eq. (29) in the form

$$\Sigma_{\nu+\omega}^\sigma - \Sigma_\nu^\sigma = -\frac{1}{\beta} \sum_{\sigma', \nu'} I_{t; \nu, \nu'}^{\sigma\sigma'; \omega} (G_{\nu'+\omega}^{\sigma'} - G_{\nu'}^{\sigma'}). \quad (C1)$$

Here, we labeled I_t by only three frequencies, chosen in the natural parametrization of the t channel, with the bosonic frequency ω as a superscript and the two fermionic frequencies ν and ν' as subscripts. We also introduce a diagrammatic representation of the WI that is slightly different from Fig. 8(c): In Fig. 25(a), we have the difference in self-energies on the left and a difference of the vertices, each contracted by a different propagator on the right. Indeed, each vertex is contracted by only the propagator corresponding to the long line. All the short, external legs are amputated; they do not contribute to the diagram. In particular, the short wavy line only serves to ensure energy conservation for each vertex; it does not enter the equation itself. We recall that dark and light colors distinguish the two spin species; dashed lines with dark and light colors symbolize a sum over spin.

If we take the limit $\omega \rightarrow \infty$ in Eq. (C1) or Fig. 25(a), the left-hand side (l.h.s.) simplifies to $-\hat{\Sigma}$, where $\hat{\Sigma}_\nu^\sigma = \Sigma_\nu^\sigma - Un_{\bar{\sigma}}$ is the self-energy without its static Hartree part. In this limit, the r.h.s. simplifies as well. First, we express I_t , the vertex

irreducible in the t channel, as a sum of the fully irreducible vertex $R_{2\text{PI}}$ and the vertices reducible in the complementary channels, γ_a and γ_p . Fully irreducible vertex diagrams beyond the bare vertex F_0 decay in all frequency arguments; therefore, $\lim_{\omega \rightarrow \infty} R = F_0$. However, F_0 makes no contribution to Eq. (C1), as it is frequency independent and thus leads to cancellation in the v' sum. In contrast to $R_{2\text{PI}}$, the reducible vertices γ_r have specific contributions that are independent of certain (fermionic) frequencies. By substituting $\gamma_a + \gamma_p$ for I_t in Eq. (C1), we get

$$\begin{aligned} \tilde{\Sigma}_v^\sigma &= \lim_{\omega \rightarrow \infty} \frac{1}{\beta} \sum_{\sigma'v'} I_{t;v+\omega,v'+\omega}^{\sigma\sigma';\omega} (G_{v'+\omega}^{\sigma'} - G_{v'}^{\sigma'}) \\ &= \lim_{\omega \rightarrow \infty} \frac{1}{\beta} \sum_{\sigma'v'} (\gamma_{a;v+\omega,v}^{\sigma\sigma';v'-v} + \gamma_{p;v+\omega,v}^{\sigma\sigma';v+v'+\omega}) (G_{v'+\omega}^{\sigma'} - G_{v'}^{\sigma'}). \end{aligned} \quad (\text{C2})$$

Here, we expressed γ_a and γ_p each in their natural frequency parametrization. As fermionic frequencies, we chose the two lower vertex legs in Fig. 25(a) for both γ_a and γ_p . The transfer frequency is $v' - v$ w.r.t. to the a channel and $v + v' + \omega$ w.r.t. to the p channel.

Next, we use the fact that a reducible vertex always decays with its bosonic transfer argument, $\lim_{\omega \rightarrow \infty} \gamma_{r;v,v'}^{\sigma\sigma';\omega} = 0$, and that a propagator G_v^σ decays as $1/v$. It follows that $\lim_{\omega \rightarrow \infty} \sum_{v'} \gamma_{a;v+\omega,v}^{\sigma\sigma';v'-v} G_{v'+\omega}^{\sigma'} = 0$, since nonzero values of γ_a require $v' \sim v$, i.e., finite v' , so that $G_{v'+\omega}^{\sigma'} \rightarrow 0$. Similarly, $\lim_{\omega \rightarrow \infty} \sum_{v'} \gamma_{p;v+\omega,v}^{\sigma\sigma';v+v'+\omega} G_{v'}^{\sigma'} = 0$, since nonzero values of γ_p require $v' \sim -\omega$, increasing in magnitude with ω , so that $G_{v'}^{\sigma'} \rightarrow 0$. By contrast, the remaining two terms in Eq. (C2) give finite contributions,

$$\tilde{\Sigma}_v^\sigma = \lim_{\omega \rightarrow \infty} \left(\frac{1}{\beta} \sum_{\sigma'v'} \gamma_{p;v+\omega,v}^{\sigma\sigma';v+\hat{v}} G_{\hat{v}}^{\sigma'} - \frac{1}{\beta} \sum_{\sigma'v'} \gamma_{a;v+\omega,v}^{\sigma\sigma';v'-v} G_{v'}^{\sigma'} \right),$$

where we relabeled $\hat{v} = v' + \omega$ in the p channel. This relation is the first equality in Fig. 25(b). The symbol “ \doteq ” here means that both sides agree up to $O(1/\omega)$, i.e., they are equal in the limit $\omega \rightarrow \infty$.

For the rest of the analysis, we refrain from spelling out the equations and proceed diagrammatically. In Fig. 25(b), lines in red colors (dark and light for the two spins) carry the large frequency ω . All of these are amputated external legs, for otherwise, the result would vanish in the limit $\omega \rightarrow \infty$. This means that only those diagrams of γ_p and γ_a contribute where the red legs directly meet at the same bare vertex. Thereby, ω is transferred without entering an actual propagator, and the result is completely independent of ω . We can gather all those diagrams by inserting the BSEs for the reducible vertices. This is done in the second equality of Fig. 25(b). The first two and last two summands per row differ by the choice of spin in the propagator loop on top of $\gamma_{a/p}$. In the BSE for $\gamma_p^{\sigma\sigma'}$, we fixed the spin σ at the bottom propagator, thus eliminating the prefactor $1/2$.

By virtue of the BSEs, we have two out-going red legs attached to I_p , and an in- and an out-going red leg attached to the left of I_a . Since I_p and I_a are irreducible in parallel and antiparallel lines, respectively, the only diagram for each that allows the red legs to meet directly is the bare vertex F_0 .

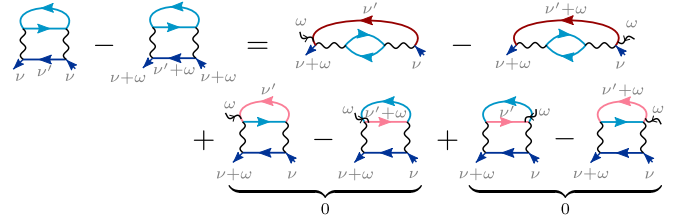


FIG. 26. The WI as in Fig. 25(a) evaluated in second-order (bold) perturbation theory. The l.h.s., $\Sigma_{v+\omega}^\sigma - \Sigma_v^\sigma$, matches the $\gamma_a^{\sigma\sigma}$ vertex contributions on the r.h.s., top row. The bottom row on the r.h.s., coming from $\gamma_a^{\sigma\hat{\sigma}}$ and $\gamma_p^{\sigma\hat{\sigma}}$ cancels. Note that $\gamma_p^{\sigma\sigma}$ has no second-order contribution; see, e.g., Fig. 5 in Ref. [101] for a collection of all second-order diagrams. We give some frequency labels for clarity. On the r.h.s., red colors mark the loop propagator contracting the vertex I_t in Fig. 25(a).

Furthermore, as F_0 is only nonzero between different spins, the result collapses to the three contributions (without any spin summation) shown in Fig. 25(c). At this point, the red lines meet at a bare vertex, and the ω dependence (and thus the wiggly line) can be simply removed. We see that the first two terms in Fig. 25(c) cancel. It remains to use the crossing symmetry of F to transform the last summand of Fig. 25(c) into the expression of Fig. 25(d). The latter is precisely the SDE (the Hartree term is absorbed in $\tilde{\Sigma}$) in the form known from Eq. (26) and Fig. 8(b).

It is no coincidence that the first two summands of Fig. 8(c) canceled, and the nonzero contribution to $\tilde{\Sigma}$ is the one from the equal-spin vertex $\gamma_a^{\sigma\sigma}$ coming from $I_t^{\sigma\sigma}$. In fact, the WI (C1) also holds without spin sum,

$$\Sigma_{v+\omega}^\sigma - \Sigma_v^\sigma = -\frac{1}{\beta} \sum_{v'} I_{t;v,v'}^{\sigma\sigma;\omega} (G_{v'+\omega}^\sigma - G_{v'}^\sigma). \quad (\text{C3})$$

For convenience, we check this explicitly at second order in U in Fig. 26. Equation (C3) can be found by deriving the WI not only using the local charge operator, $\hat{\rho}_1 = \sum_\sigma \hat{n}_\sigma$, but also the local spin operator $\hat{\rho}_2 = \sum_\sigma \tau_{\sigma\sigma}^z \hat{n}_\sigma$, where τ^z is the third Pauli matrix. For the latter, the WI reads

$$\Sigma_{v+\omega}^\sigma - \Sigma_v^\sigma = -\frac{1}{\beta} \sum_{\sigma'v'} \tau_{\sigma'\sigma'}^z I_{t;v,v'}^{\sigma\sigma';\omega} (G_{v'+\omega}^{\sigma'} - G_{v'}^{\sigma'}). \quad (\text{C4})$$

Summing Eqs. (C1) and (C4), one obtains Eq. (C3).

3. Envelope diagrams in the WI

The vertex in the PA deviates from the exact vertex starting at fourth order in the bare interaction U . Through the SDE, the self-energy is exact up to order U^4 , while errors start at order U^5 . *A priori*, one thus expects the PA to violate the WI to order U^4 , as induced by the missing U^4 vertex diagrams—the so-called envelope diagrams. However, it could also happen that this specific class of vertex diagrams does not contribute to the WI, i.e., that the envelope diagrams cancel out in Eq. (29). Indeed, numerically, we found the PA to violate the WI to order U^5 instead of U^4 . In this section, we show analytically that in the special case of particle-hole and spin symmetry, the envelope diagrams cancel in the WI.

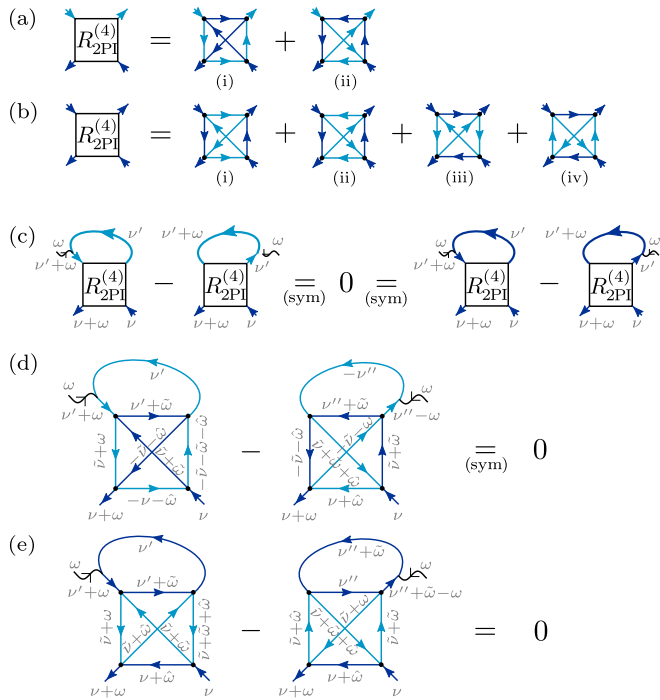


FIG. 27. R_{2PI} at order U^4 (envelope diagrams) with (a) different and (b) equal spins on the external legs. (c) Under particle-hole and spin symmetry, $R_{2PI}^{(4)}$ does not contribute to the WI. This is because pairs of diagrams cancel in the difference of Eq. (29), as apparent after a suitable transformation $\nu' \rightarrow \nu''$ in, say, the second term. (d) Cancellation of diagrams (i) and (ii) from (a) inserted in the first and second term of the WI. (e) Same for diagrams (iii) and (iv) from (b).

Figures 27(a) and 27(b) show the envelope diagrams with different and equal spins (distinguished by light and dark colors) on the external legs, respectively. (For brevity, we collapsed the interaction line to a dot). These diagrams can also be found in Figs. 14 and 15 of Ref. [40]. Together, they form the fully irreducible vertex R_{2PI} at fourth order in U ; $R_{2PI}^{(4)\sigma\bar{\sigma}}$ has two and $R_{2PI}^{(4)\sigma\sigma}$ four diagrams, as enumerated by Roman

numbers. Figure 27(c) states that neither $R_{2PI}^{(4)\sigma\bar{\sigma}}$ nor $R_{2PI}^{(4)\sigma\sigma}$ contribute to the WI given particle-hole and spin symmetry.

Indeed, using $G_v^\sigma = -G_{-v}^\sigma$ and $G_v^\uparrow = G_v^\downarrow$, one can always find pairs of envelope diagrams that cancel in the subtraction inherent to the WI. This cancellation becomes apparent after suitably transforming the summation frequency in, say, the second term of the WI (thus changing ν' to ν''). In Figs. 27(d) and 27(e), we establish the cancellation by explicitly writing frequency labels on all internal lines.

Figure 27(d) considers the case of $R_{2PI}^{(4)\sigma\bar{\sigma}}$ with diagram (i) and (ii) in the first and second term of the WI, respectively. The same set of frequency labels occurs in both terms, differing at most by minus signs. Both terms have a total of three global minus signs in their frequency labels; using $G_v^\sigma = -G_{-v}^\sigma$, these minus signs can be pulled out of the equation. One obtains a mathematically identical expression for both terms and thus a vanishing difference. The case of $R_{2PI}^{(4)\sigma\bar{\sigma}}$ with diagram (ii) in the first and diagram (i) in the second term proceeds analogously. Indeed, one can transform one case into the other by flipping the arrows on the two horizontal and the two diagonal lines (accordingly changing $\nu \rightarrow -\nu$ on their frequency labels) and suitably changing the spin labels. The cancellation works just as before. Further, the cancellation also works for diagrams (i) and (ii) of $R_{2PI}^{(4)\sigma\sigma}$ (again for both orders). In this case, one must further invoke spin symmetry, $G_v^\uparrow = G_v^\downarrow$.

Finally, Fig. 27(e) treats the case of $R_{2PI}^{(4)\sigma\sigma}$ with diagram (iii) and (iv) in the first and second term of the WI, respectively. The argumentation is the same as before. Thanks to the transformation $\nu' \rightarrow \nu''$ in the second term, one has a mathematically identical expression for both terms and thus a vanishing difference. Again, interchanging the role of diagrams (iii) and (iv) in the two terms of the WI merely amounts to flipping the arrows; here, this affects the two vertical and the two diagonal lines, all of which have spin $\bar{\sigma}$. As apparent from Fig. 27(e), no minus signs are involved, and matching pairs of frequency labels also have the same spins. The cancellation of diagrams (iii) and (iv) thus works also in the absence of particle-hole or spin symmetry.

[1] D. Sénéchal, A.-M. Tremblay, and C. Bourbonnais, eds., *Theoretical Methods for Strongly Correlated Electrons* (Springer-Verlag, New York, 2004), pp. 237–296.

[2] S. X. Yang, H. Fotsso, J. Liu, T. A. Maier, K. Tomko, E. F. D’Azevedo, R. T. Scalettar, T. Pruschke, and M. Jarrell, Parquet approximation for the 4×4 Hubbard cluster, *Phys. Rev. E* **80**, 046706 (2009).

[3] K.-M. Tam, H. Fotsso, S.-X. Yang, T.-W. Lee, J. Moreno, J. Ramanujam, and M. Jarrell, Solving the parquet equations for the Hubbard model beyond weak coupling, *Phys. Rev. E* **87**, 013311 (2013).

[4] A. Valli, T. Schäfer, P. Thunström, G. Rohringer, S. Andergassen, G. Sangiovanni, K. Held, and A. Toschi, Dynamical vertex approximation in its parquet implementation: Application to Hubbard nanorings, *Phys. Rev. B* **91**, 115115 (2015).

[5] G. Li, N. Wentzell, P. Pudleiner, P. Thunström, and K. Held, Efficient implementation of the parquet equations: Role of the reducible vertex function and its kernel approximation, *Phys. Rev. B* **93**, 165103 (2016).

[6] N. Wentzell, G. Li, A. Tagliavini, C. Taranto, G. Rohringer, K. Held, A. Toschi, and S. Andergassen, High-frequency asymptotics of the vertex function: Diagrammatic parametrization and algorithmic implementation, *Phys. Rev. B* **102**, 085106 (2020).

[7] R. A. Smith, Planar version of Baym-Kadanoff theory, *Phys. Rev. A* **46**, 4586 (1992).

[8] V. Janiš, A. Kauch, and V. Pokorný, Thermodynamically consistent description of criticality in models of correlated electrons, *Phys. Rev. B* **95**, 045108 (2017).

[9] F. B. Kugler and J. von Delft, Derivation of exact flow equations from the self-consistent parquet relations, *New J. Phys.* **20**, 123029 (2018).

[10] W. Metzner, M. Salmhofer, C. Honerkamp, V. Meden, and K. Schönhammer, Functional renormalization group approach to correlated fermion systems, *Rev. Mod. Phys.* **84**, 299 (2012).

- [11] M. Salmhofer, *Renormalization - An Introduction*, edited by R. Balian, W. Beiglböck, H. Grosse, E. H. Lieb, N. Reshetikhin, H. Spohn, and W. Thirring (Springer-Verlag, Berlin, 1999).
- [12] J. Berges, N. Tetradis, and C. Wetterich, Non-perturbative renormalization flow in quantum field theory and statistical physics, *Phys. Rep.* **363**, 223 (2002).
- [13] P. Kopietz, L. Bartosch, and F. Schütz, *Introduction to the Functional Renormalization Group* (Springer, Berlin, 2010).
- [14] N. Dupuis, L. Canet, A. Eichhorn, W. Metzner, J. Pawłowski, M. Tissier, and N. Wschebor, The nonperturbative functional renormalization group and its applications, *Phys. Rep.* **910**, 1 (2021).
- [15] F. B. Kugler and J. von Delft, Multiloop functional renormalization group for general models, *Phys. Rev. B* **97**, 035162 (2018).
- [16] F. B. Kugler and J. von Delft, Multiloop Functional Renormalization Group That Sums Up All Parquet Diagrams, *Phys. Rev. Lett.* **120**, 057403 (2018).
- [17] A. A. Katanin, Fulfillment of Ward identities in the functional renormalization group approach, *Phys. Rev. B* **70**, 115109 (2004).
- [18] T. Enss, Renormalization, Conservation Laws and Transport in Correlated Electron Systems, Ph.D. thesis, University of Stuttgart, 2016.
- [19] K. Veschgini and M. Salmhofer, Schwinger-Dyson renormalization group, *Phys. Rev. B* **88**, 155131 (2013).
- [20] M. Caltapanides, D. M. Kennes, and V. Meden, Finite-bias transport through the interacting resonant level model coupled to a phonon mode: A functional renormalization group study, *Phys. Rev. B* **104**, 085125 (2021).
- [21] F. Schütz, L. Bartosch, and P. Kopietz, Collective fields in the functional renormalization group for fermions, Ward identities, and the exact solution of the Tomonaga-Luttinger model, *Phys. Rev. B* **72**, 035107 (2005).
- [22] L. Bartosch, H. Freire, J. J. R. Cardenas, and P. Kopietz, A functional renormalization group approach to the Anderson impurity model, *J. Phys.: Condens. Matter* **21**, 305602 (2009).
- [23] S. Streib, A. Isidori, and P. Kopietz, Solution of the Anderson impurity model via the functional renormalization group, *Phys. Rev. B* **87**, 201107(R) (2013).
- [24] J. Diekmann and S. G. Jakobs, Parquet approximation and one-loop renormalization group: Equivalence on the leading-logarithmic level, *Phys. Rev. B* **103**, 155156 (2021).
- [25] C. Karrasch, M. Pletyukhov, L. Borda, and V. Meden, Functional renormalization group study of the interacting resonant level model in and out of equilibrium, *Phys. Rev. B* **81**, 125122 (2010).
- [26] C. Karrasch, S. Andergassen, M. Pletyukhov, D. Schuricht, L. Borda, V. Meden, and H. Schoeller, Non-equilibrium current and relaxation dynamics of a charge-fluctuating quantum dot, *Europhys. Lett.* **90**, 30003 (2010).
- [27] D. M. Kennes and V. Meden, Interacting resonant-level model in nonequilibrium: Finite-temperature effects, *Phys. Rev. B* **87**, 075130 (2013).
- [28] D. M. Kennes, D. Schuricht, and V. Meden, Efficiency and power of a thermoelectric quantum dot device, *Europhys. Lett.* **102**, 57003 (2013).
- [29] V. Meden, W. Metzner, U. Schollwöck, and K. Schönhammer, Scaling behavior of impurities in mesoscopic Luttinger liquids, *Phys. Rev. B* **65**, 045318 (2002).
- [30] V. Meden, S. Andergassen, W. Metzner, U. Schollwöck, and K. Schönhammer, Scaling of the conductance in a quantum wire, *Europhys. Lett.* **64**, 769 (2003).
- [31] S. Andergassen, T. Enss, V. Meden, W. Metzner, U. Schollwöck, and K. Schönhammer, Functional renormalization group for Luttinger liquids with impurities, *Phys. Rev. B* **70**, 075102 (2004).
- [32] V. Meden, T. Enss, S. Andergassen, W. Metzner, and K. Schönhammer, Correlation effects on resonant tunneling in one-dimensional quantum wires, *Phys. Rev. B* **71**, 041302(R) (2005).
- [33] T. Enss, V. Meden, S. Andergassen, X. Barnabé-Thériault, W. Metzner, and K. Schönhammer, Impurity and correlation effects on transport in one-dimensional quantum wires, *Phys. Rev. B* **71**, 155401 (2005).
- [34] S. Andergassen, T. Enss, V. Meden, W. Metzner, U. Schollwöck, and K. Schönhammer, Renormalization-group analysis of the one-dimensional extended Hubbard model with a single impurity, *Phys. Rev. B* **73**, 045125 (2006).
- [35] V. Meden, S. Andergassen, T. Enss, H. Schoeller, and K. Schönhammer, Fermionic renormalization group methods for transport through inhomogeneous Luttinger liquids, *New J. Phys.* **10**, 045012 (2008).
- [36] A. Tagliavini, C. Hille, F. B. Kugler, S. Andergassen, A. Toschi, and C. Honerkamp, Multiloop functional renormalization group for the two-dimensional Hubbard model: Loop convergence of the response functions, *SciPost Phys.* **6**, 009 (2019).
- [37] C. Hille, F. B. Kugler, C. J. Eckhardt, Y.-Y. He, A. Kauch, C. Honerkamp, A. Toschi, and S. Andergassen, Quantitative functional renormalization group description of the two-dimensional Hubbard model, *Phys. Rev. Research* **2**, 033372 (2020).
- [38] T. Schäfer, N. Wentzell, F. Šimkovic, Y.-Y. He, C. Hille, M. Klett, C. J. Eckhardt, B. Arzhang, V. Harkov, F.-M. Le Régent, A. Kirsch, Y. Wang, A. J. Kim, E. Kozik, E. A. Stepanov, A. Kauch, S. Andergassen, P. Hansmann, D. Rohe, Y. M. Vilk *et al.*, Tracking the Footprints of Spin Fluctuations: A MultiMethod, MultiMessenger Study of the Two-Dimensional Hubbard Model, *Phys. Rev. X* **11**, 011058 (2021).
- [39] E. Gull, A. J. Millis, A. I. Lichtenstein, A. N. Rubtsov, M. Troyer, and P. Werner, Continuous-time Monte Carlo methods for quantum impurity models, *Rev. Mod. Phys.* **83**, 349 (2011).
- [40] G. Rohringer, A. Valli, and A. Toschi, Local electronic correlation at the two-particle level, *Phys. Rev. B* **86**, 125114 (2012).
- [41] A. Tagliavini, S. Hummel, N. Wentzell, S. Andergassen, A. Toschi, and G. Rohringer, Efficient Bethe-Salpeter equation treatment in dynamical mean-field theory, *Phys. Rev. B* **97**, 235140 (2018).
- [42] G. Rohringer, H. Hafermann, A. Toschi, A. A. Katanin, A. E. Antipov, M. I. Katsnelson, A. I. Lichtenstein, A. N. Rubtsov, and K. Held, Diagrammatic routes to nonlocal correlations beyond dynamical mean field theory, *Rev. Mod. Phys.* **90**, 025003 (2018).
- [43] J. Lichtenstein, D. Sánchez de la Peña, D. Rohe, E. Di Napoli, C. Honerkamp, and S. Maier, High-performance functional

- Renormalization Group calculations for interacting fermions, *Comput. Phys. Commun.* **213**, 100 (2017).
- [44] C. J. Eckhardt, C. Honerkamp, K. Held, and A. Kauch, Truncated unity parquet solver, *Phys. Rev. B* **101**, 155104 (2020).
- [45] R. Hedden, V. Meden, T. Pruschke, and K. Schönhammer, A functional renormalization group approach to zero-dimensional interacting systems, *J. Phys.: Condens. Matter* **16**, 5279 (2004).
- [46] C. Karrasch, R. Hedden, R. Peters, T. Pruschke, K. Schönhammer, and V. Meden, A finite-frequency functional renormalization group approach to the single impurity Anderson model, *J. Phys.: Condens. Matter* **20**, 345205 (2008).
- [47] S. G. Jakobs, M. Pletyukhov, and H. Schoeller, Nonequilibrium functional renormalization group with frequency-dependent vertex function: A study of the single-impurity Anderson model, *Phys. Rev. B* **81**, 195109 (2010).
- [48] A. Isidori, D. Roosen, L. Bartosch, W. Hofstetter, and P. Kopietz, Spectral function of the Anderson impurity model at finite temperatures, *Phys. Rev. B* **81**, 235120 (2010).
- [49] J. F. Rentrop, V. Meden, and S. G. Jakobs, Renormalization group flow of the Luttinger-Ward functional: Conserving approximations and application to the Anderson impurity model, *Phys. Rev. B* **93**, 195160 (2016).
- [50] N. K. Yirga and D. K. Campbell, Frequency-dependent functional renormalization group for interacting fermionic systems, *Phys. Rev. B* **103**, 235165 (2021).
- [51] P. Chalupa, T. Schäfer, M. Reitner, D. Springer, S. Andergassen, and A. Toschi, Fingerprints of the Local Moment Formation and its Kondo Screening in the Generalized Susceptibilities of Many-Electron Problems, *Phys. Rev. Lett.* **126**, 056403 (2021).
- [52] D. Vilardi, C. Taranto, and W. Metzner, Antiferromagnetic and d -wave pairing correlations in the strongly interacting two-dimensional Hubbard model from the functional renormalization group, *Phys. Rev. B* **99**, 104501 (2019).
- [53] P. M. Bonetti, A. Toschi, C. Hille, S. Andergassen, and D. Vilardi, Single-boson exchange representation of the functional renormalization group for strongly interacting many-electron systems, *Phys. Rev. Research* **4**, 013034 (2022).
- [54] A. Georges, G. Kotliar, W. Krauth, and M. J. Rozenberg, Dynamical mean-field theory of strongly correlated fermion systems and the limit of infinite dimensions, *Rev. Mod. Phys.* **68**, 13 (1996).
- [55] R. Bulla, T. A. Costi, and T. Pruschke, Numerical renormalization group method for quantum impurity systems, *Rev. Mod. Phys.* **80**, 395 (2008).
- [56] C. Taranto, S. Andergassen, J. Bauer, K. Held, A. Katanin, W. Metzner, G. Rohringer, and A. Toschi, From Infinite to Two Dimensions through the Functional Renormalization Group, *Phys. Rev. Lett.* **112**, 196402 (2014).
- [57] N. Wentzell, C. Taranto, A. Katanin, A. Toschi, and S. Andergassen, Correlated starting points for the functional renormalization group, *Phys. Rev. B* **91**, 045120 (2015).
- [58] P. W. Anderson, Localized magnetic states in metals, *Phys. Rev.* **124**, 41 (1961).
- [59] A. Hewson, *The Kondo Problem to Heavy Fermions* (Cambridge University Press, Cambridge, 1993).
- [60] P. Chalupa, P. Gunacker, T. Schäfer, K. Held, and A. Toschi, Divergences of the irreducible vertex functions in correlated metallic systems: Insights from the Anderson impurity model, *Phys. Rev. B* **97**, 245136 (2018).
- [61] P. Coleman, *Introduction to Many-Body Physics* (Cambridge University Press, Cambridge, 2015).
- [62] C. Honerkamp, D. Rohe, S. Andergassen, and T. Enss, Interaction flow method for many-fermion systems, *Phys. Rev. B* **70**, 235115 (2004).
- [63] A. Eberlein, Fermionic two-loop functional renormalization group for correlated fermions: Method and application to the attractive Hubbard model, *Phys. Rev. B* **90**, 115125 (2014).
- [64] M. Rück and J. Reuther, Effects of two-loop contributions in the pseudofermion functional renormalization group method for quantum spin systems, *Phys. Rev. B* **97**, 144404 (2018).
- [65] J. Thoenniss, M. K. Ritter, F. B. Kugler, J. von Delft, and M. Punk, Multiloop pseudofermion functional renormalization for quantum spin systems: Application to the spin- $\frac{1}{2}$ kagome Heisenberg model, [arXiv:2011.01268](https://arxiv.org/abs/2011.01268).
- [66] D. Kiese, T. Mueller, Y. Iqbal, R. Thomale, and S. Trebst, Multiloop functional renormalization group approach to quantum spin systems, [arXiv:2011.01269](https://arxiv.org/abs/2011.01269).
- [67] The translation of the notation used in this work to the notation used in many other works, among them Ref. [42], is the following: The diagrammatic channels relate to one another as $a = ph$, $p = pp$, $t = ph$; the vertex two-particle reducible in channel r is referred to as $\gamma_r = \Phi_r$, the vertex irreducible in channel r as $I_r = \Gamma_r$ and the fully two-particle irreducible vertex as $R_{2PI} = \Lambda_{irr}$.
- [68] C. Hille, D. Rohe, C. Honerkamp, and S. Andergassen, Pseudogap opening in the two-dimensional Hubbard model: A functional renormalization group analysis, *Phys. Rev. Research* **2**, 033068 (2020).
- [69] M. Wallerberger, A. Hausoel, P. Gunacker, A. Kowalski, N. Parragh, F. Goth, K. Held, and G. Sangiovanni, w2dynamics: Local one- and two-particle quantities from dynamical mean field theory, *Comput. Phys. Commun.* **235**, 388 (2019).
- [70] A. C. Hewson and D. Meyer, Numerical renormalization group study of the Anderson-Holstein impurity model, *J. Phys.: Condens. Matter* **14**, 427 (2002).
- [71] P. Coleman, Heavy fermions: Electrons at the edge of magnetism, in *Handbook of Magnetism and Advanced Magnetic Materials*, edited by H. Kronmüller and S. Parkin. Vol 1: Fundamentals and Theory (John Wiley, Hoboken, NJ, 2007).
- [72] C. Watzenböck, M. Edelmann, D. Springer, G. Sangiovanni, and A. Toschi, Characteristic Timescales of the Local Moment Dynamics in Hund's Metals, *Phys. Rev. Lett.* **125**, 086402 (2020).
- [73] L. Gaspard and J. M. Tomczak, Timescale of local moment screening across and above the Mott transition, [arXiv:2112.02881](https://arxiv.org/abs/2112.02881).
- [74] C. Watzenböck, M. Fellingner, K. Held, and A. Toschi, Long-term memory magnetic correlations in the Hubbard model: A dynamical mean-field theory analysis, [arXiv:2112.02903](https://arxiv.org/abs/2112.02903).
- [75] E. Kozik, M. Ferrero, and A. Georges, Nonexistence of the Luttinger-Ward Functional and Misleading Convergence of Skeleton Diagrammatic Series for Hubbard-Like Models, *Phys. Rev. Lett.* **114**, 156402 (2015).
- [76] O. Gunnarsson, G. Rohringer, T. Schäfer, G. Sangiovanni, and A. Toschi, Breakdown of Traditional Many-Body

- Theories for Correlated Electrons, *Phys. Rev. Lett.* **119**, 056402 (2017).
- [77] M. Reitner, P. Chalupa, L. Del Re, D. Springer, S. Ciuchi, G. Sangiovanni, and A. Toschi, Attractive Effect of a Strong Electronic Repulsion: The Physics of Vertex Divergences, *Phys. Rev. Lett.* **125**, 196403 (2020).
- [78] T. Schäfer, G. Rohringer, O. Gunnarsson, S. Ciuchi, G. Sangiovanni, and A. Toschi, Divergent Precursors of the Mott-Hubbard Transition at the Two-Particle Level, *Phys. Rev. Lett.* **110**, 246405 (2013).
- [79] V. Janiš and V. Pokorný, Critical metal-insulator transition and divergence in a two-particle irreducible vertex in disordered and interacting electron systems, *Phys. Rev. B* **90**, 045143 (2014).
- [80] T. Ribic, G. Rohringer, and K. Held, Nonlocal correlations and spectral properties of the Falicov-Kimball model, *Phys. Rev. B* **93**, 195105 (2016).
- [81] T. Schäfer, S. Ciuchi, M. Wallerberger, P. Thunström, O. Gunnarsson, G. Sangiovanni, G. Rohringer, and A. Toschi, Non-perturbative landscape of the Mott-Hubbard transition: Multiple divergence lines around the critical endpoint, *Phys. Rev. B* **94**, 235108 (2016).
- [82] J. Vučičević, N. Wentzell, M. Ferrero, and O. Parcollet, Practical consequences of the Luttinger-Ward functional multivaluedness for cluster DMFT methods, *Phys. Rev. B* **97**, 125141 (2018).
- [83] P. Thunström, O. Gunnarsson, S. Ciuchi, and G. Rohringer, Analytical investigation of singularities in two-particle irreducible vertex functions of the Hubbard atom, *Phys. Rev. B* **98**, 235107 (2018).
- [84] D. Springer, P. Chalupa, S. Ciuchi, G. Sangiovanni, and A. Toschi, Interplay between local response and vertex divergences in many-fermion systems with on-site attraction, *Phys. Rev. B* **101**, 155148 (2020).
- [85] C. Melnick and G. Kotliar, Fermi-liquid theory and divergences of the two-particle irreducible vertex in the periodic Anderson lattice, *Phys. Rev. B* **101**, 165105 (2020).
- [86] S. Adler (unpublished).
- [87] Y. M. Vilk and A.-M. S. Tremblay, Non-perturbative many-body approach to the Hubbard model and single-particle pseudogap, *J. Phys. I (France)* **7**, 1309 (1997).
- [88] G. Rohringer and A. Toschi, Impact of non-local correlations over different energy scales: A dynamical vertex approximation study, *Phys. Rev. B* **94**, 125144 (2016).
- [89] The QMC result was obtained using w2dynamics [69] with Worm sampling [98,99] and symmetric improved estimators [100], designed to reduce the high-frequency noise, see further Appendix B 3. However, the noise cannot be suppressed completely, and thus the QMC result fluctuates around the PA and mfRG solution.
- [90] F. Krien, E. G. C. P. van Loon, H. Hafermann, J. Otsuki, M. I. Katsnelson, and A. I. Lichtenstein, Conservation in two-particle self-consistent extensions of dynamical mean-field theory, *Phys. Rev. B* **96**, 075155 (2017).
- [91] F. Krien, Conserving dynamical mean-field approaches to strongly correlated systems, Ph.D. thesis, Universität Hamburg, 2018.
- [92] H. Hafermann, E. G. C. P. van Loon, M. I. Katsnelson, A. I. Lichtenstein, and O. Parcollet, Collective charge excitations of strongly correlated electrons, vertex corrections, and gauge invariance, *Phys. Rev. B* **90**, 235105 (2014).
- [93] G. Baym, Self-consistent approximations in many-body systems, *Phys. Rev.* **127**, 1391 (1962).
- [94] P. Kopietz, L. Bartosch, L. Costa, A. Isidori, and A. Ferraz, Ward identities for the Anderson impurity model: Derivation via functional methods and the exact renormalization group, *J. Phys. A: Math. Theor.* **43**, 385004 (2010).
- [95] A. Toschi, A. A. Katanin, and K. Held, Dynamical vertex approximation: A step beyond dynamical mean-field theory, *Phys. Rev. B* **75**, 045118 (2007).
- [96] T. Ayrál and O. Parcollet, Mott physics and collective modes: An atomic approximation of the four-particle irreducible functional, *Phys. Rev. B* **94**, 075159 (2016).
- [97] C. U. Hille, The role of the self-energy in the functional renormalization group description of interacting Fermi systems, Ph.D. thesis, Eberhard Karls Universität Tübingen, 2020.
- [98] P. Gunacker, M. Wallerberger, E. Gull, A. Hausoel, G. Sangiovanni, and K. Held, Continuous-time quantum Monte Carlo using worm sampling, *Phys. Rev. B* **92**, 155102 (2015).
- [99] P. Gunacker, M. Wallerberger, T. Ribic, A. Hausoel, G. Sangiovanni, and K. Held, Worm-improved estimators in continuous-time quantum Monte Carlo, *Phys. Rev. B* **94**, 125153 (2016).
- [100] J. Kaufmann, P. Gunacker, A. Kowalski, G. Sangiovanni, and K. Held, Symmetric improved estimators for continuous-time quantum Monte Carlo, *Phys. Rev. B* **100**, 075119 (2019).
- [101] F. B. Kugler, Counting Feynman diagrams via many-body relations, *Phys. Rev. E* **98**, 023303 (2018).